Design and optimization of a geothermal absorption cooling system in a tropical climate

Charles Maragna, Amín Altamirano, Brice Tremeac, Florent Fabre, Laurène Rouzic, Pierre Barcellini

▶ **To cite this version:**

Charles Maragna, Amín Altamirano, Brice Tremeac, Florent Fabre, Laurène Rouzic, et al.. Design and optimization of a geothermal absorption cooling system in a tropical climate. Applied Energy, 2024, 364, pp.123102. 10.1016/j.apenergy.2024.123102 . hal-04536943

HAL Id: hal-04536943

https://brgm.hal.science/hal-04536943v1

Submitted on 8 Apr 2024

HAL is a multi-disciplinary open access archive for the deposit and dissemination of scientific research documents, whether they are published or not. The documents may come from teaching and research institutions in France or abroad, or from public or private research centers.

L'archive ouverte pluridisciplinaire **HAL**, est destinée au dépôt et à la diffusion de documents scientifiques de niveau recherche, publiés ou non, émanant des établissements d'enseignement et de recherche français ou étrangers, des laboratoires publics ou privés.

Distributed under a Creative Commons Attribution 4.0 International License

Applied Energy 364 (2024) 123102

Contents lists available at ScienceDirect

Applied Energy

journal homepage: www.elsevier.com/locate/apenergy

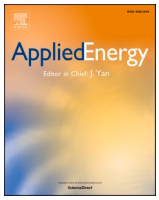

Design and optimization of a geothermal absorption cooling system in a tropical climate

Charles Maragna [a,*], Amín Altamirano [b], Brice Tréméac [b], Florent Fabre [c], Laurène Rouzic [c], Pierre Barcellini [c]

[a] BRGM, F-45060 Orléans, France
[b] Laboratoire du froid et des systèmes énergétiques et thermiques (Lafset), Conservatoire national des arts et métiers, HESAM Université, F-75003 Paris, France
[c] Etamine, F-44000 Nantes, France

HIGHLIGHTS

- A geothermal absorption chiller in tropical climate is modelled.
- The influence of design parameters on electricity consumption is investigated.
- The system undergoes multi-objective optimization.
- The well proximity and geothermal temperature are keys to the system relevance.

ARTICLE INFO

Keywords:
Air conditioning
Tropical climate
Absorption chiller
Geothermal energy
Surrogate modelling
Energy system optimization

ABSTRACT

The electricity required for air conditioning is soaring worldwide. Absorption chillers represent an alternative to classical vapor compression systems, using heat instead of electricity. However, absorption chillers powered by renewable geothermal heat have received little attention so far. This paper introduces a system using a hot geothermal fluid (typically in the range of 80–110 °C) to produce cooling through a single-effect absorption chiller, and Domestic Hot Water (DHW) through a heat exchanger. It considers a hotel located in Martinique, a French Caribbean island. The electric consumption of every subsystem has been thoroughly estimated. The originality of this paper is twice: i) the system is modelled in TRNSYS software considering dynamic conditions, ii) the system undergoes surrogate modelling and multi-objective optimization to minimize both the cost and the CO_2 content of the delivered thermal energy. Several scenarios are considered, depending upon the geothermal temperature, mass flow rate, well remoteness, and demand size. The studied system appears to be systematically more expensive than a combination of a classical vapor compression chiller and a boiler for DHW. However, it can significantly decrease the CO_2 content of the provided energy, especially in an island where most electricity is generated from fossil fuels. The proximity of the geothermal well and the use of the warm water leaving the absorption generator (here for DHW production) appear to be key factors for system relevance, along with a hotter geothermal fluid (e.g., 110 °C instead of 80 °C).

1. Introduction

In 2016, the International Energy Agency estimated that the use of Air Conditioners (AC) and electric fans to keep buildings cool accounted for 2000 $TWh.y^{-1}$, i.e., nearly 20% of the total electricity used in buildings around the world; this number may soar to 6200 $TWh.y^{-1}$by 2050 [1]. The Global Warming Potential (GWP) over the whole lifecycle of an AC installation (including electricity consumption) is especially high in Caribbean Islands, where most electricity is generated through fossil fuels combustion, though geothermal resources have been proved to exist. For instance, a recent energy audit of 55 office buildings in Martinique, a French Caribbean island, showed that 47% of their electricity consumption is used for air conditioning [2]. Meanwhile, in 2023, the only geothermal power plant operated in the Caribbean is located in Bouillante, Guadeloupe [3]. The 15 MWe plant is fed by a 250 °C geothermal fluid and covers 6% of the electricity demand of the island. Besides, indirect measurements suggest that geological formations in

* Corresponding author at: BRGM, 3 av. Claude-Guillemin BP 36009, 45060 Orléans Cedex 2, France.
E-mail address: c.maragna@brgm.fr (C. Maragna).

https://doi.org/10.1016/j.apenergy.2024.123102
Received 28 August 2023; Received in revised form 4 March 2024; Accepted 23 March 2024
Available online 2 April 2024
0306-2619/© 2024 The Authors. Published by Elsevier Ltd. This is an open access article under the CC BY license (http://creativecommons.org/licenses/by/4.0/).

Nomenclature[1]

Latin letters

c	intensive cost (e.g. per energy)
C	cost [€]
E	energy [MWh]
L	length of the buried twin pipes [m]
M	mass [kg]
$\dot{m}$	mass flow rate [$kg \cdot h^{-1}$]
r	radius [m]
t	time [h]
T	temperature [°C]
$\mathscr{p}$	pressure per unit length of pipe [$Pa \cdot m^{-1}$]
$\mathscr{P}$	pressure [Pa]
Q	heat transfer [MWh]
$\dot{Q}$	heat transfer rate [W]
v	speed [$m \cdot s^{-1}$]
W	work transfer [MWh]
$\dot{W}$	power [W]

Greek letters

δT	temperature pinch of a heat exchanger [°C]
λ	thermal conductivity [$W \cdot K^{-1}.m^{-1}$]
ρ	density [$kg \cdot m^{-3}$]
ρC_p	volumetric heat capacity [$J \cdot K^{-1}m^{-3}$]
γ	intensive Global Warming Potential (e.g. per energy)
Γ	Global Warming Potential [$kgCO_2eq$]

Subscripts

b	borehole
GTH	geothermal
$demand$	total demand (cooling + DHW)
el	electric
ev	evaporator
ext	external
gen	generator
in	inlet
int	intermediate temperature source of the absorption chiller
nom	nominal condition
out	outlet
p	pipe (of the buried twin pipes)
$sorp$	absorption chiller

Superscripts

$\dot{u}$	time derivative of u
u^*	dimensionless quantity u
E^*	energy normalized by the total demand $E^* = \frac{E}{Q_{cooling}+Q_{DHW}}$
$E^{\sim}$	energy normalized by the cooling demand $E^{\sim} = \frac{E}{Q_{cooling}}$

Abbreviations

AC	air conditioner
ACC	air-cooled chiller
COP	coefficient of performance
CT	cooling tower
DHW	domestic hot water
EER	energy efficiency ratio
GP	Gaussian process
GWP	global warming potential
HX	heat exchanger
KPI	key performance indicator
ldb	lower dead band of a logical processor
ORC	organic Rankine cycle
PE	polyethylene
PV	photovoltaic
RMSE	root mean square error
SDR	standard dimensional ratio
udb	upper dead band of a logical processor

[1] The units between brackets are to be used for the numerical applications throughout the paper.

Lamentin sector, Martinique, may contain geothermal fluids at 400–800 m depth at a temperature in the range 80–110 °C. Such a fluid may be used in a sorption chiller to produce cooling.

Sorption cooling systems represent an alternative to the classical vapor compression systems since they use heat instead of electricity to produce the cooling effect. They can run on renewable heat (e.g., solar, geothermal and biomass) or waste heat, thereby decreasing the CO_2 emissions related to cooling [4,5]. These chillers can be divided into two broad categories: closed-cycle (when the refrigerant fluid is not in direct contact with the cooled air, e.g., absorption and adsorption chillers) and open-cycle (when the refrigerant fluid is in direct contact with the cooled air, e.g., Desiccant Evaporative Cooling or DEC systems). A previous review study by the authors indicated that DEC and adsorption systems possess the smallest market share of commercial sorption chillers (7% and 9–11%, respectively) given their drawbacks related to either elevated costs, variable cooling power, low COP, ambient condition limitations, sanitary risks, or low cooling power density [4]. On the other hand, absorption chillers (with a market share of 82–84%), are the most popular given their performance, compactness, and investment cost [4,5]. For this reason, the present study focuses on the absorption chiller technology.

A typical single-stage absorption chiller (Fig. 1) consists of an evaporator, a condenser, an absorber, a generator (also referred to as desorber), a circulation pump, a liquid-to-liquid exchanger (also referred to as a solution heat exchanger), and two expansion valves. The chiller operates as follows: heat is applied to the solution in the generator ($\dot{Q}_{gen}$), causing it to release refrigerant vapor (i.e., water vapor) through desorption. This vapor then moves to the condenser where it releases heat ($\dot{Q}_{con}$) and is condensed into liquid form. The liquid water then flows through a throttle valve and is vaporized again at low pressure and temperature in the evaporator. This evaporation process absorbs heat from the cold source ($\dot{Q}_{ev}$). The created vapor is then absorbed by the solution (poor in refrigerant) in the cooled absorber ($\dot{Q}_{abs}$). The solution, now rich in refrigerant, is then pumped from the absorber to the generator to start the cycle again. A solution exchanger (SHX) is placed between the absorber and the generator to recover internal heat, thereby improving the chiller's efficiency. Finally, if a volatile solution such as ammonia-water is used, a vapor purification system (commonly called a "rectifier") must be installed between the generator and the condenser to increase the purity of the refrigerant circuit. The excess heat produced at an intermediary temperature is $\dot{Q}_{int} = \dot{Q}_{cond} + \dot{Q}_{abs}$.

Regarding the working fluids in commercial systems, only two options are available: Ammonia/Water (NH_3/H_2O, being ammonia the refrigerant and water the absorbent), preferred when temperatures below 0 °C are needed, and Water/Lithium Bromide (H_2O/LiBr, being water the refrigerant and water the absorbent), preferred for building AC or applications where positive cooling is required since this working pair exhibits higher thermal Coefficient of Performance (COP_{th}) [6]. Overall, the H_2O/LiBr seems like the predominant working fluid on the market [7] and has been considered for this study.

The use of geothermal energy to produce cooling through absorption chillers has already received some attention in recent times. For instance, Wang et al. performed a detailed economic viability analysis of a geothermal absorption chiller for a university in Western Australia, though they did not investigate to which extent the chiller performance

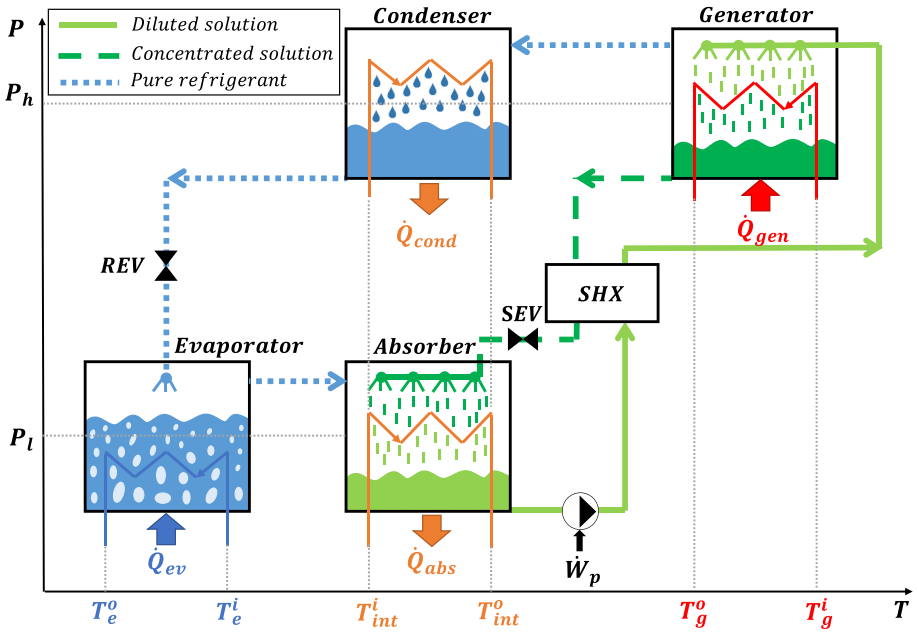

Fig. 1. Single-effect absorption chiller.

depends upon the geothermal fluid temperature [8]. Han et al. studied a H_2O/LiBr double-effect absorption cooling system powered by a geothermal fluid at 150 °C. They estimated the thermal COP to be above 1.0 [9]. Tetemke et al. designed an NH_3/H_2O absorption chiller to cool down drinking water from 37.8 °C to 16.0 °C [10]. They reported a thermal COP of 0.30, a typical value according to the authors for the NH_3/H_2O working fluid with relatively low geothermal source temperature (83 °C) [6]. Saucedo-Velázquez et al. simulated the retrofit of deep boreholes in closed-loop (Borehole Heat Exchangers) to produce cooling through a half-effect, a single-effect, a double-effect, or a triple-effect absorption chiller [11]. For geothermal driving temperatures in the range of 59–80 °C, 77–110 °C, 135–162 °C, and 180–187 °C, respectively, the cooling systems could deliver chilled water temperatures around 8 °C. In 2006, an NH_3/H_2O chiller was installed in Chena, Alaska, to produce cooling at −29 °C with a geothermal resource at 74 °C; a river at +4 °C cooled down the sorption chiller [12]. Finally, Gado et al. reviewed hybrid sorption-vapor compression cooling systems, classifying the systems as cascade, partially integrated and fully integrated systems [13]. They reported that this combination would allow an electricity consumption reduction of about 45–88% in comparison with conventional vapor compression systems.

Innovative architectures to produce cooling, heating, electricity, soft water or even hydrogen with solar and geothermal energy have been designed and modelled (see Table 1). However, these simulations are often carried out under steady-state conditions, though the performances of a single-effect absorption chiller are impacted by the fluctuating operative conditions. To the authors' knowledge, the dynamic behavior of a single-effect geothermal absorption chiller has been poorly studied.

This paper intends to fill this knowledge gap in the Caribbean context. The present work is organized as follows (see Fig. 2): Section 2.1 describes the system and its dynamic modelling. Section 2.2 gives further insight of the system components for a preliminary, non-optimal sizing, while section 2.3 introduces the key performance indictors considered throughout the paper. Section 3 reports the results of the simulations for the preliminary sizing and a sensitivity analysis in the vicinity of this sizing, changing one or two parameters at a time. Section 4 discusses the multi-objective optimization of the system for several technical and economic scenarios.

2. Materials and methods

2.1. System modelling

2.1.1. Overall system description

The designed system encompasses two geothermal wells (one for pumping, one for reinjection), a single-effect absorption chiller, a backup Air-Cooled Chiller (ACC), a Cooling Tower (CT), three-way valves (diverters and mixers), pumps, heat exchangers, and additional tanks (see Fig. 3).

The geothermal fluid extracted from a geothermal well (point 1) enters the source side of the heat exchanger HX_1 (point 2 in Fig. 3). It transfers heat to water entering the load side of HX_1 (points 6 and 4). The load side is connected to a buffer tank Tank_1 through a buried pipe, and then to the generator inlet of the absorption chiller (point 14). Tank_1 adds inertia to the model, making its numerical convergence easier.

The cooled water leaving the generator (point 15) flows to a buffer tank Tank_2 (point 18) and transfers heat through HX_2 for Domestic Hot Water (DHW) preparation.

When operated, the flow rates in pumps 3 and 5 (P_3 and P_5, respectively) are $\dot{m} = 5 \left\langle \dot{m}_{DHW} \right\rangle$, where $\left\langle \dot{m}_{DHW} \right\rangle$ is the daily mean of the required DHW flow rate and $\dot{m}_{DHW}$ the instantaneous required DHW flow rate (see §2.1.2). If the water temperature exiting the DHW tank Tank_3 (point 57) does not reach the setpoint $T_{59} = T_{sp\ DHW} = 40$ °C, then an electrical backup heater is turned on, consuming $\dot{Q}_{DHW}^{backup}$. Meanwhile, the intermediate temperature source of the absorption chiller is connected to a buffer tank (Tank_4) that leads to a Cooling Tower (CT).

The evaporator of the absorption chiller and the ACC are connected to the cooling tank (Tank_5), from which cooled water is distributed into the building (point 47). The set point departure in the cooling emitters is $T_{47} = 7$ °C, with water flowing back at $T_{48} = 12$ °C.

The role of the valves mix_i and div_i ($i = 1$ to 5) will be further explained in §2.2.7.

The system is modelled in TRNSYS v18 [23,24]. TRNSYS is a program for the dynamic simulation of transient systems. At every time step, TRNSYS iteratively solves the temperature and flow rate of every node of the system. Its modular structure and graphical interface allows the user to easily connect so-called "Types", i.e. modules describing the

Table 1
Some systems using geothermal heat for cooling through absorption chillers

Reference	Source			Use						System	Location	Findings	Simulation [(a)]
	Geothermal	PV	Solar thermal	Dehumidification	Cooling	Heating	Electricity	Desalinization	Hydrogen				
[14]	x				x		x	x	x			Better prediction of KPIs with improved machine learning techniques	S
[15]	x		x		x	x	x	x		Absorption cooling system with LiBr-H_2O	Iran	Payback period of 6 years	S
[16]	x		x		x	x	x			Combined ejector-absorption refrigeration cycle	Yukon territory, Canada	Overall energetic and exergetic efficiencies 53% and 37% respectively	S
[17]	x				x					Single effect absorption cooling system with NH_3-H_2O couple	Izmir, Turkey	COP ≈ 0.44; Payback period between 6 and 9 years	S
[18]	x			x	x	x				Absorption refrigeration cycle & liquid dehumidification cycle with LiBr-H2O and LiCl-H2O		Heating capacity decreases by 50% with the reinjection temperature increasing from 70 to 80 °C	S
[19]	x				x	x	x			Modified absorption refrigeration cycle and a Kalina cycle using NH_3-H_2O mixture	Germany	Maximization of exergy efficiency or minimization of exergy destruction	S
[20]	x	x	x		x	x	x			ORC and H_2O/LiBr absorption chiller	Campi Flegrei (Naples, South Italy)	Lower payback with PV compared with solar thermal	D
[21]	x						x			Novel parallel double-effect absorption power cycle with H_2O/LiBr		Power output increased by 41%, cost decreased by 10%	S
[22]	x				x		x			Modified Kalina Cycle and absorption refrigeration cycle with NH_3/H_2O		Cost 13–20% lower than Kalina Cycle separated from absorption cooling system	S

[a] : S: Under static conditions; D: under dynamic conditions

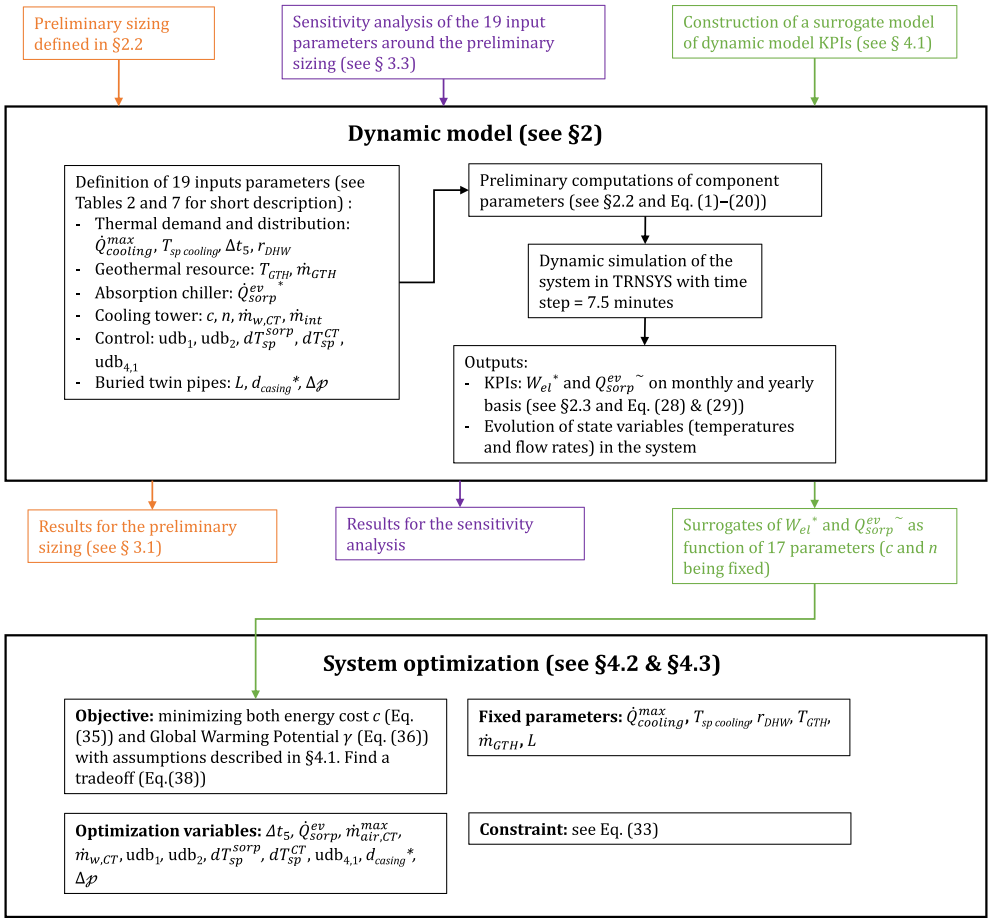

Fig. 2. Flowchart of the research reported in this paper.

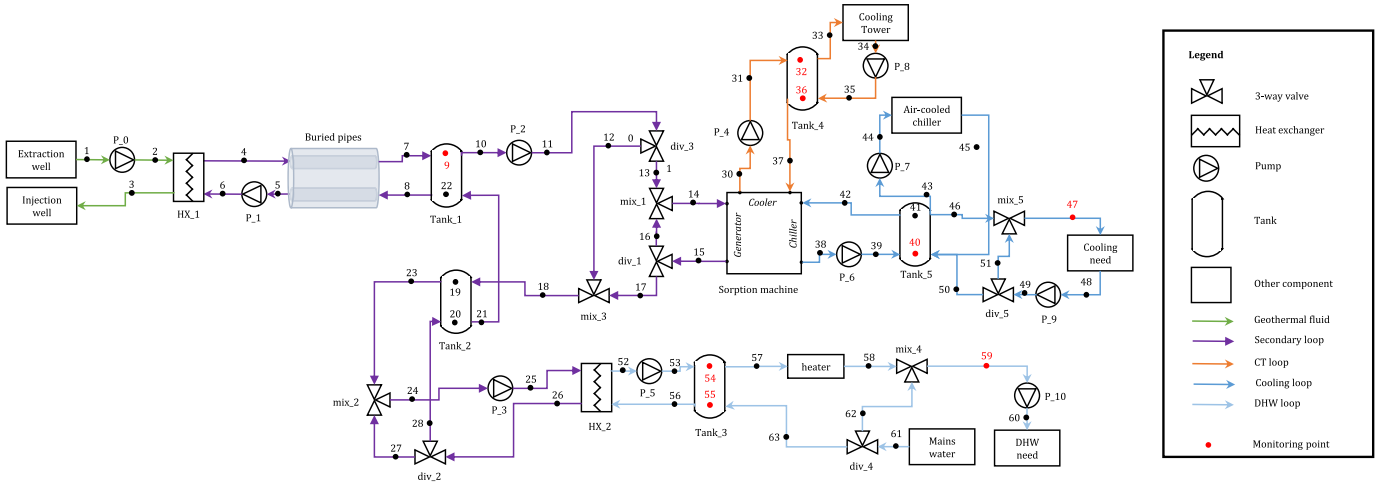

Fig. 3. Hydraulic diagram of the studied system. "0" or "1" close to div_3 indicates the effective outlet depending on the status of microprocessor #3 (see 2.2.7).

physical behavior of the system components, and to define control strategies. The software comes with dozens of standard Types, additional Types from the Ground Heat Pump and Storage Tank libraries edited by TESS have been used for this work [25]. As pointed out in [26], the main limitations of TRNSYS are high development costs of user-defined Types and its incapability to natively deal with hydraulics (i.e. TRNSYS computes flow rates rather than pressures and resulting flow rates). Modelica/Dymola is widely used as an alternative, though the computational costs are reported to be higher [27]. Here the time step is $\Delta t = 7.5$ min and the system is simulated for 1 year, after a simulated few days have been discarded to account for the initial transient behavior of the building. Note that all Types except the buried pipes (Type951) and tanks (Type1534) assume the components have no inertia, and internal transient phenomena are overlooked.

2.1.2. *Thermal energy requirement*

A 5173 m^2 (floor area) hotel located in Fort-de-France, Martinique, France, welcoming up to 365 guests was considered (see Supplementary

Material for further description). The tropical climate consists of two main seasons: a relatively mild and dry season from January to mid-April, and a hot and wet season from July to November (see Fig. 4). The hotel was modelled in TRNSYS considering weather data forecast by 2050 and the RCP4.5 scenario of the Intergovernmental Panel on Climate Change. The cooling requirement was estimated to $Q_{cooling}$ = 570.5 MWh/y with a peak load $\dot{Q}^{max}_{cooling}$ of 104.3 kW. The monthly cooling need is minimum in January at 43.6 MWh and reaches a maximum of 56.3 MWh in August. The Domestic Hot Water (DHW) need was estimated to Q_{DHW} = 90.0 MWh/y, assuming every guest requires 125 L/day (that is $\left\langle \dot{m}_{DHW} \right\rangle$ = 5.2 kg.h^{-1}) at $T_{sp\ DHW} = T_{59}$ = 40 °C, with hourly modulations, provided that the mains water varies between 30.0 °C in January and 33.3 °C in August. The need for cooling ($Q_{cooling}$) in 2050 is expected to be 9% higher than that of 2020, whereas the need for DHW (Q_{DHW}) is expected to decrease by 11.2% in the same period of time.

2.2. Components

The constitutive parameters of the components are reported in Table 2. Altogether, the values reported in Table 2 define a "preliminary sizing" whose simulation is reported in section 3.1. The preliminary sizing might not be optimal, but illustrate the system behavior. The system optimization is addressed in section 4.

2.2.1. Geothermal resource

The geothermal resource is characterized by an available (constant) mass flow rate $\dot{m}_{GTH} = \dot{m}_1 = \dot{m}_2$ and a temperature $T_{GTH} = T_1 = T_2$, assuming a volumetric fluid heat capacity of 4.15 MJ.K^{-1}.m^{-3} [28]. The counterflow heat exchanger HX_1 decouples the geothermal mass flow rate $\dot{m}_{GTH}$ (the source side) from the generator mass flow rate $\dot{m}_{gen}$ (the load side). For a given geothermal flow rate, an increase in the cold stream mass flow rate ($\dot{m}_{gen}$) leads to an increase in the exchanger heat rate (see Fig. 5a). This, however, leads to a decrease in the temperature of the fluid stream that goes back to the generator (as illustrated in Fig. 5b), causing a decrease in the absorption chiller's thermal COP. For this reason, there is an optimal ratio $\dot{m}_{GTH}/\dot{m}_{gen}$, as discussed in sections 3.2 and 4. Note that in Fig. 5a, the heat losses through the buried pipe are overlooked so that $T_4 = T_{14}$ and $T_6 = T_{15}$. As $\dot{m}_{GTH}/\dot{m}_{gen}$ varies, the heat transfer coefficient of the exchanger is computed with the NTU-ε method to ensure a pinch of δT= 2 °C [29], a typical value for geothermal heat exchangers. The inequality $\dot{m}_{GTH} \leq \dot{m}_{gen}$ implies that $T_3 - T_6 = \delta T$. A cold stream temperature difference $T_4 - T_6$ = 5 °C is applied, as this is typical for the generator of the absorption chiller considered in 2.2.3.

2.2.2. Buried pipes

Insulated twin pipes of length L are buried at a depth of 1.0 m (see Fig. 6). These pipes convey hot water from the geothermal heat exchanger to the absorption chiller. Prior to the simulation, the inner diameter of the pipes $d_{int,p}$ is dimensioned to ensure a linear pressure drop $\Delta\mathscr{P}$ (see Eq. (1)) per pipe of 100 Pa.m^{-1}.

$$\Delta_{\mathscr{P}} = \frac{\Delta\mathscr{P}}{L} = \frac{f\rho}{2d_{int,p}}v^2 \tag{1}$$

With $v = \frac{\pi}{4}\frac{\dot{m}_{4\to7}}{\rho}\frac{d_{int,p}{}^2}{4} = \frac{\pi}{4}\frac{\dot{m}_{8\to5}}{\rho}\frac{d_{int,p}{}^2}{4}$ the fluid velocity [m.s^{-1}], ρ the fluid density [kg.m^{-3}] and f the friction factor [−]. The friction factor depends on the liquid's flow regime, determined by the Reynolds number Re (see Eq. (2)). if $Re < 3000$, the friction factor can be calculated using Eq. (3), otherwise, it can be calculated using Eq. (4).

$$Re = \frac{\rho v d_{int,p}}{\mu} \tag{2}$$

$$f_{lam} = \frac{64}{Re} \tag{3}$$

$$\frac{1}{\sqrt{f_{turb}}} = -2log\left(\frac{\varepsilon}{3.7d_{int,p}} + \frac{2.51}{Re\sqrt{f_{turb}}}\right) \tag{4}$$

The Standard Dimensional Ratio (SDR), i.e., the ratio of the outside pipe diameter $d_{ext,p}$ to the wall thickness e_p, is assumed to be 11. Therefore, $d_{ext,p} = \frac{d_{int}}{1-\frac{2}{SDR}}$ and $e_p = \frac{d_{ext}-d_{int}}{2}$. Besides, the casing diameter d_{casing} and the center-to-center pipe spacing a_p are derived from geometric ratios as $d_{casing} = d_{casing}{}^* \bullet d_{ext,p}$ and $a_p = a^* \bullet d_{ext,p}$ with $d_{casing}{}^* = 3$ and $a^* = 1.5$ (see Fig. 6). The thermal conductivities of the pipe material and the fill insulation are 0.4 W·K^{-1}.m^{-1} and 0.04 W·K^{-1}.m^{-1}, respectively. The soil thermal conductivity and heat capacity are assumed to be 1.8 W·K^{-1}.m^{-1} and 2.10 MJ.K^{-1}.m^{-1} [30]. For the preliminary sizing, a negligible pipe length of 1.0 m is considered. In other words, the absorption chiller is right at the edge of the geothermal well.

As the variations of monthly median values of $T_{dry\ bulb}$ are only about 3 °C, it is assumed that the annual temperature variations at a depth of 1.0 m are damped. Type951 considers that the pipe is encompassed in an equivalent cylinder of soil whose diameter equals the pipe depth and that a temperature is applied on the cylinder boundary, emulating the temperature at the ground surface. Here a constant temperature of 26 °C has been applied, which is somehow lower than the air dry bulb temperature used for the building simulation (see Fig. 4). However, the discrepancy shall not significantly affect the heat losses from the buried pipe since the heat-carrier fluid is much warmer than the air (typically, the temperature of the heat-carrier fluid is a few °C below the

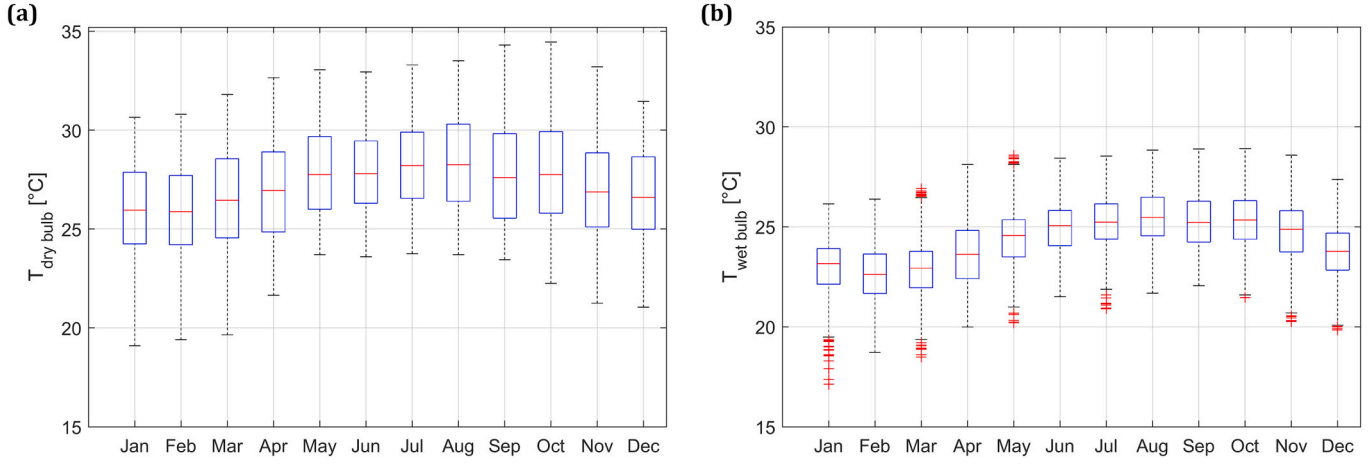

Fig. 4. Monthly boxplots forecast of (a) dry bulb and (b) wet bulb temperatures at Fort-de-France in 2050 according to RCP4.5 scenario of the IPCC

Table 2
Constitutive parameters of the components and values used for the preliminary sizing.

Component	TRNSYS Type	Parameter	Value
Geothermal resource	Equation	Temperature (T_{GTH})	80 °C
		Mass flow rate ($\dot{m}_{GTH}$)	25.84 × 10^3 kg.h^{-1}
		Specific mass flow rate ($\dot{m}_{GTH}/\dot{Q}^{max}_{cooling}$)	68.57 kg. MJ^{-1}
Buried pipes	951	Length (L)	1 m
		Nominal linear pressure drop (Δ_{P}) per pipe	100 Pa.m^{-1}
		Inner diameter of pipes ($d_{int,p}$)	6.67 cm
		Outer diameter of pipes ($d_{ext,p}$)	8.15 cm
		Center-to-center pipe spacing (a_p)	10.90 cm
		Diameter of casing material (d_{casing})	24.45 cm
		Normalized center-to-center pipe spacing ($a^* = \frac{a}{d_{ext,p}}$)	1.5
		Normalized casing diameter ($d_{casing}{}^* = \frac{d_{casing}}{d_{ext,p}}$)	3.0
Absorption chiller	127	Nominal cooling capacity $\dot{Q}^{ev}_{sorp}$	104.3 kW
		Normalized nominal cooling power ($\dot{Q}^{ev}_{sorp}{}^* = \frac{\dot{Q}^{ev}_{sorp}}{\dot{Q}^{max}_{cooling}}$)	1
		Auxiliary electrical consumption ($\dot{Q}^{elec}_{sorp}$) (see eq. *(9)*)	0.32 kW
		Chiller's total mass M_{sorp} (see eq. *(10)*)	1430 kg
		Mass flow rate at generator ($\dot{m}^{gen}_{sorp}$)	25.84 × 10^3 kg.h^{-1}
		Mass flow rate at the evaporator ($\dot{m}^{ev}_{sorp}$)	16.43 × 10^3 kg.h^{-1}
		Mass flow rate at the chiller's heat sink ($\dot{m}^{int}_{sorp}$)	54.93 × 10^3 kg.h^{-1}
Cooling tower	162	Mass transfer constant (c)	1.3
		Mass transfer exponent (n)	0.6
		Maximum air mass flow rate ($\dot{m}^{max}_{air,CT}$)	54.93 × 10^3 kg.h^{-1}
		Water mass flow rate ($\dot{m}_{w,CT}$)	54.93 × 10^3 kg.h^{-1}
		Fan electrical consumption at maximum air flow ($\dot{W}^{max}_{el,fan}$)	4.23 kW
		Pump power ($\dot{W}_{pump\ CT}$)	1.66 kW
Air-cooled chiller	118	Nominal cooling capacity $\dot{Q}^{ev}_{ACC}$	104.3 kW
Tank_1	1534	Volume (V_1)	12.92 m^3
		Equivalent storage duration (Δt_1)	0.25 h
Tank_3	1534	Volume (V_3)	0.48 m^3
		Equivalent storage duration (Δt_3)	0.25 h
Tank_4	1534	Volume (V_4)	27.34 m^3
		Equivalent storage duration (Δt_4)	0.25 h
Tank_5	1534	Volume (V_5)	8.18 m^3
		Equivalent storage duration (Δt_5)	0.5 h

geothermal fluid temperature, see Fig. 10c).

2.2.3. Absorption chiller

A black box model is used to characterize the aborption chiller's behavior. Data from the Yazaki manufacturer's catalogues for their SC series (nominal cooling capacities $\left(\dot{Q}^{ev}_{sorp}\right)_{nom}$ from 35.2 kW to 175 kW) was used for the model fitting [31]. The entire dataset includes 832 operating conditions in the temperature ranges of $5^\circ C \le T_{ev,out} \le 13^\circ C$, $24^\circ C \le T_{int,in} \le 32^\circ C$, and $70^\circ C \le T_{gen,in} \le 95^\circ C$. The nominal condition of these models is defined at $T^{nom}_{ev,out} = 7^\circ C$, $T^{nom}_{int,in} = 31^\circ C$, and $T^{nom}_{gen,in} = 88^\circ C$ for a thermal COP_{th} of 0.700. Note that at these nominal conditions, the thermal COP reaches 38.0% of the maximum theoretical COP (Carnot COP), defined in Eq. *(5)* [32]:

$$COP^{Carnot}_{th} = \left(\frac{T^{nom}_{gen,in} - T^{nom}_{int,in}}{T^{nom}_{gen,in}}\right) \bullet \left(\frac{T^{nom}_{ev,out}}{T^{nom}_{int,in} - T^{nom}_{ev,out}}\right) \quad (5)$$

With the numerical application of Eq. (5) being $COP^{Carnot}_{th} = \left(\frac{88-31}{273.15+88}\right) \bullet \left(\frac{273.15+7}{31-7}\right) = 1.84$. In order to regroup the different commercial models in a single dataset, the heat rate at the evaporator $\dot{Q}^{ev}_{sorp}$ and generator $\dot{Q}^{gen}_{sorp}$ were normalized for their respective values at the nominal conditions $\left(\dot{Q}^{ev}_{sorp}\right)_{nom}$ and $\left(\dot{Q}^{gen}_{sorp}\right)_{nom}$. Finally, a Gaussian Process (GP) regression technique was used to model the cooling rate as a function of $T_{ev,out}$, $T_{int,in}$ and $T_{gen,in}$ (see Appendix A for theoretical background). The model results are in reasonably good agreement with the dataset (see Fig. 7a), as indicated by the 5-fold cross-validation Root Mean Square Errors (RMSE) of 0.055 and 0.061 for the evaporator and generator normalized powers, respectively.

Using a subset of the dataset restricted to machines with $\left(\dot{Q}^{ev}_{sorp}\right)_{nom} = 35.2$ kW, the authors had previously derived linear fits of $\dot{Q}^{ev}_{sorp}$ and $\dot{Q}^{gen}_{sorp}$ as functions of $T_{ev,out}$, $T_{int,in}$ and $T_{gen,in}$ [33]. After elementary manipulations, they can be expressed as:

$$\frac{\dot{Q}^{ev}_{sorp}}{\left(\dot{Q}^{ev}_{sorp}\right)_{nom}} = -0.0795 + 0.0170 \cdot T_{ev,out} - 0.0883 \cdot T_{int,in} + 0.0414 \cdot T_{gen,in} \quad (6)$$

$$\frac{\dot{Q}^{gen}_{sorp}}{\left(\dot{Q}^{gen}_{sorp}\right)_{nom}} = -0.0157 + 0.0160 \cdot T_{ev,out} - 0.0832 \cdot T_{int,in} + 0.0390 \cdot T_{gen,in} \quad (7)$$

In Eq. *(6)* and *(7)*, temperatures are expressed in °C. The RMSE calculated over the full dataset are then respectively 0.135 for eq. *(6)* and 0.101 for eq. *(7)*. In other words, the newly fitted GPs outperform the linear fits.

When activated, the absorption chiller (Type 127) modulates the cooling heat rate $\dot{Q}^{ev}_{sorp}$ to ensure it meets the desired set point (see section 2.2.7). The resulting partial load decreases the thermal COP of the chiller, as observed in Fig. 7b.

Crystallization is a common risk in H_2O/LiBr systems. In order to prevent any crystallization risk in the simulated system, Eq. *(8)* was developed to indicate the maximum inlet generator temperature (function of the chilled water and intermediate temperatures) that can be employed. This equation has been derived from a thermodynamic model of the absorption chiller (assuming steady-state, thermodynamic equilibrium conditions, and a pinch of 5 °C between the internal fluids and the heat transfer fluids) [34], the equilibrium thermodynamic properties of the H_2O/LiBr couple [35] and the crystallization limit of the solution [36]:

$$T^{max}_{gen,in} = min\left(95, 58.67 + 0.121 \bullet T_{ev,out} + 1.215 \bullet T_{int,in}\right) \quad (8)$$

The inlet generator temperature is modulated by the recirculation valves mix_1 and div_1. Besides, the following equations for the electric power required by the absorption chiller ($\dot{W}^{el}_{sorp}$) and the chiller's mass M_{abs} are deduced from the manufacturer datasheets [31]:

$$\dot{W}^{el}_{sorp} = 0.334 \bullet \dot{Q}^{ev}_{sorp}{}^{0.592} \quad (9)$$

$$M_{abs} = 0.0162 \bullet \dot{Q}^{ev}_{sorp} \quad (10)$$

Note that Eq. (9) $\dot{W}^{el}_{sorp}$ accounts for the electric consumption of the internal solution circulation pump and electronic devices. The chiller's mass will be used to estimate the chiller's GWP and investment and

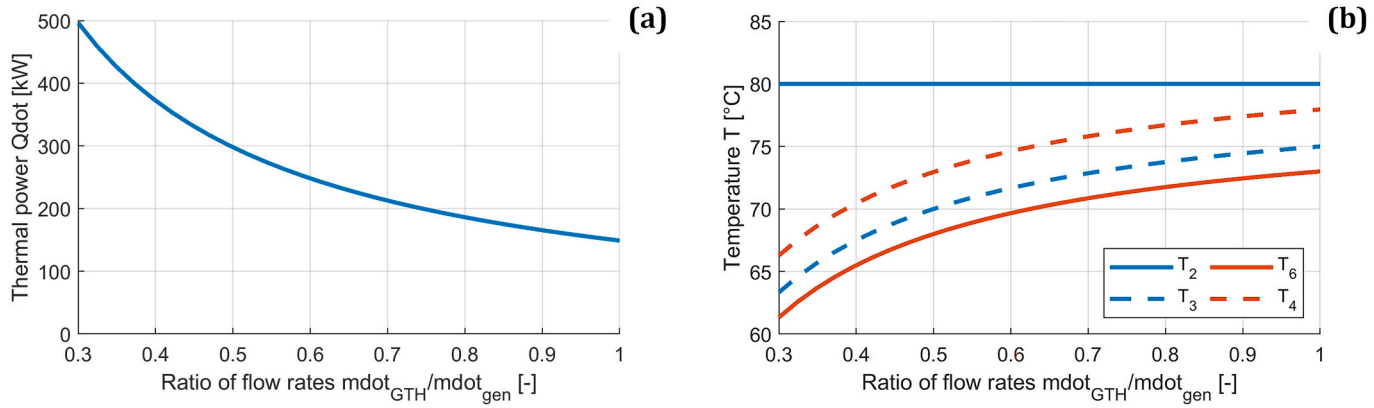

Fig. 5. Illustration of **(a)** HX_1 Heat rate and **(b)** i/o fluid streams' temperatures as a function of the ratio of the geothermal mass flow rate $\dot{m}_{GTH}$ to the generator mass flow rate $\dot{m}_{gen}$. $T_{GTH} = 80\ ^{\circ}C$; $T_3 - T_6 = 2^{\circ}C$; $T_4 - T_6 = 5^{\circ}C$.

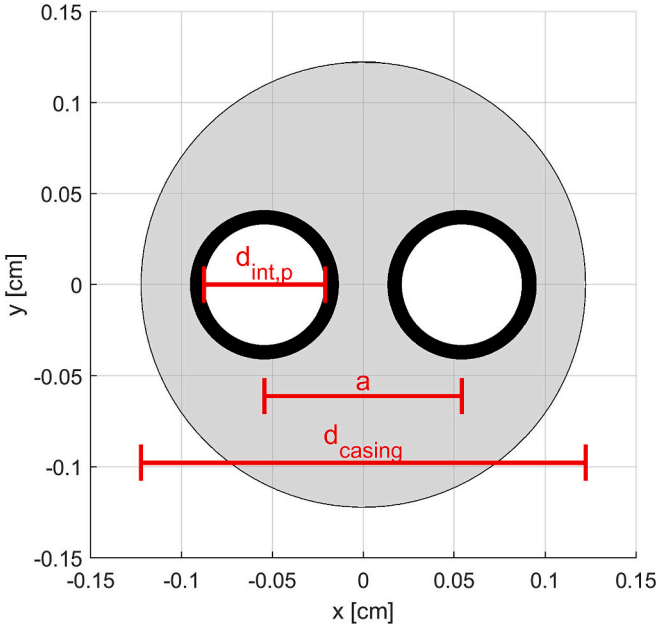

Fig. 6. Cross-sectional view of the twin pipes in the insulating casing.

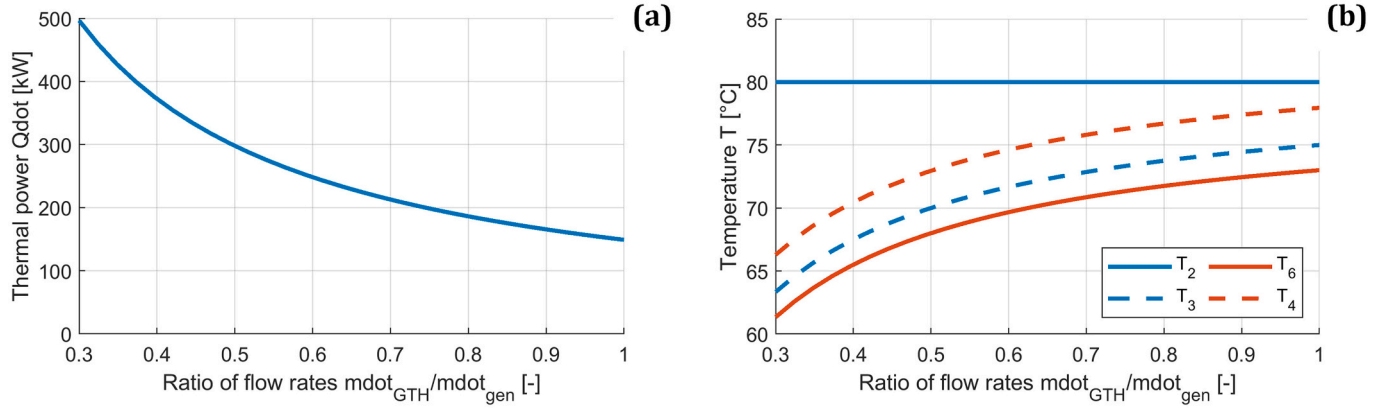

Fig. 7. *Yazaki SC series absorption chillers modelling results.* ***(a)*** *Comparison of the normalized evaporator and generator heat rates* $\dot{Q}_{sorp}^{ev\ *}$ *and* $\dot{Q}_{sorp}^{gen\ *}$ and **(b)** effect of the partial load on the thermal COP.

maintenace costs (see Table 8).

2.2.4. Cooling tower

In a direct-contact wet Cooling Tower (CT), a hot water stream is in direct contact with an air stream. Water, which is injected at the top of the CT through an exchange surface enhancement distribution method (e.g., spray nozzles), flows downwards as it is cooled through sensible and latent heat transfers. The cooled water is collected into a sump before leaving the CT. The air may enter a CT in two different flow configurations: counterflow, in which it enters at the bottom, and crossflow, in which it enters at the side [37]. As extensively reported in the literature [37,38], the transfer capability of the CT can be characterized through the Merkel number and the NTU:

$$\mathrm{Me} = c\left(\frac{\dot{m}_{w,CT}}{\dot{m}_{air,CT}}\right)^{-n} \tag{11}$$

$$\mathrm{NTU} = \frac{{}_D A_v V_{cell}}{\dot{m}_{air,CT}} = c\left(\frac{\dot{m}_{w,CT}}{\dot{m}_{air,CT}}\right)^{-n+1} \tag{12}$$

Where c and n are two constants, $\dot{m}_w$ and $\dot{m}_{air}$ the water and air mass flow rates respectively

[kg.s^{-1}], h_D the mass transfer coefficient [kg.m^{-2}.s^{-1}], A_v the surface area of water droplets per unit volume of the tower [m^2.m^{-3}], V_{cell} the volume of tower [m^3]. In addition to Eqs. (11)–(12), the ε-NTU equation developed by Jaber and Webb allows to find the thermal power retrieved from the air stream [39]. The electric power requirements of the fan and the water pump at the maximum air flow rate are estimated through Eq. (13) and Eq. (14) respectively, where the flow rates $\dot{m}$ are in kg.h^{-1}:

$$\dot{W}^{el}_{fan,max} = 0.0569 \bullet \dot{m}^{max}_{air,CT} \tag{13}$$

$$\dot{W}^{el}_{P\_8} = \frac{\dot{m}_{gen}\,\Delta\mathscr{P}_{33-34}}{0.75 \bullet \rho} \tag{14}$$

With $\Delta\mathscr{P}_{33-34} = 15$ kPa a typical value for water pressure drop in CT [40]. Type162 accounting for the cooling tower operates the fan so that the water outlet targets a desired set point $T^{CT}_{sp} = T_{wet\ bulb} + dT^{CT}_{sp}$ with dT^{CT}_{sp} the CT "approach", without exceeding the maximum air flow rate. The fan electric power consumption is then given by the cubic law (Eq. (13)):

$$\dot{W}^{el}_{fan} = \dot{W}^{el}_{fan,max} \times \left(\frac{\dot{m}_{air,CT}}{\dot{m}^{max}_{air,CT}}\right)^3 \tag{15}$$

Many CT characterizations have been reported in the literature (see Table 3). The authors have chosen those of [41] for the present work. For the preliminary sizing, the maximum air flow rate ($\dot{m}^{max}_{air,CT}$) and water flow rate $\dot{m}_{w,CT}$ are set equal to $\dot{m}_{int} = 54.93 \times 10^3$ kg.h^{-1}.

2.2.5. Air-cooled chiller (ACC)

The Energy Efficiency Ratio (EER) of the ACC is modelled with Eq. (16) based on the catalog data of the LG manufacturer [48] (see Fig. 8a)

$$\begin{aligned} EER &= \frac{\dot{Q}^{ev}_{ACC}}{\dot{W}^{el}_{ACC}} \\ &= 5.11 + 0.135 \bullet T_{sp\ outlet} - 0.0728 \bullet T_{dry\ bulb} - 0.00165 \bullet T_{dry\ bulb} \\ &\quad \bullet T_{sp\ outlet} \end{aligned} \tag{16}$$

In Eq. (16), $\dot{Q}^{ev}_{ACC}$ and $\dot{W}^{el}_{ACC}$ represent the cooling load and electric power consumption, respectively, whereas $T_{dry\ bulb}$ and $T_{sp\ outlet}$ represent the dry bulb and setpoint temperatures respectively. The ACC modulates its power to ensure it meets the desired setpoint $T_{sp\ outlet}$ (see section 2.2.7), resulting in lowered EER at partial load (see Fig. 8b).

If the absorption chiller and the ACC fail at meeting the cooling load, then some extra cooling $\dot{Q}^{missing}_{cooling}$ must be added to the system.

$$\dot{Q}^{missing}_{cooling} = \dot{Q}_{cooling} - \dot{Q}^{sorption}_{cooling} - \dot{Q}^{AC}_{cooling} \tag{17}$$

For all simulations, the missing cooling $Q^{missing}_{cooling}$ is negligible (typically $Q^{missing}_{cooling} \approx 10^{-3} \cdot \dot{Q}_{cooling}$).

2.2.6. Tanks, heat exchangers and pumps

All tanks are covered with an insulating layer (λ= 0.04 W·K^{-1}.m^{-1} and e = 10 cm). The volume V_i can be expressed as an equivalent storage duration Δt_i, i.e., the ratio of the mass of water ρV_i to the nominal flow rate (Eq. (18))

$$\Delta t_1 = \frac{\rho V_1}{\dot{m}_{gen}};\ \Delta t_3 = \frac{\rho V_3}{\left\langle \dot{m}_{DHW} \right\rangle};\ \Delta t_4 = \frac{\rho V_4}{\dot{m}_{w,CT}};\ \Delta t_5 = \frac{\rho V_5}{\dot{m}_{cooling}} \tag{18}$$

As Δt_i is an intensive quantity, it makes the comparison of systems of different scales easier. The volume of tank_2 is negligible.

Table 3
Summary of the characterization of different Cooling Towers in the literature.

Coefficient c	Exponent n	Investigated $\frac{\dot{m}_w}{\dot{m}_a}$ range	Geometry	Comments	Reference
1.3	0.77	0.25–3	Counterflow	Designed for direct evaporative cooling in mild climate	[42]
1.42	0.43		Counterflow		[43]
1.3	0.6		Counterflow		[41]
0.855	0.480	0.25–2	Counterflow		Saravel manufacturer [a]
0.342	0.253	0.3–3	Counterflow	Vertical PVC corrugated packing	[44]
0.224	0.295	0.3–3	Counterflow	Horizontal PVC corrugated packing	[44]
0.10	2.12	0.333–0.856	Counterflow/parallel flow	Air intake at the CT top to avoid the emission of airborne particles to the atmosphere	[45]
0.491	0.344	0.209–0.734	Counterflow/parallel flow		[46]
0.557	0.516	0.2–2.0	Counterflow	No drift eliminator	[47]
0.518	0.516	0.3–2.0	Counterflow	Drift eliminator A	[47]
0.593	0.573	0.3–2.0	Counterflow	Drift eliminator B	[47]
0.522	0.463	0.3–2.0	Counterflow	Drift eliminator C	[47]
0.586	0.733	0.3–2.0	Counterflow	Drift eliminator D	[47]
0.669	0.6	0.8–3.0	Counterflow	Drift eliminator E	[47]
0.67	0.525	0.8–3.0	Counterflow	Drift eliminator F	[47]

[a] Derived from manufacturer datasheets (http://www.saravel.com/products.php?en&id=73).

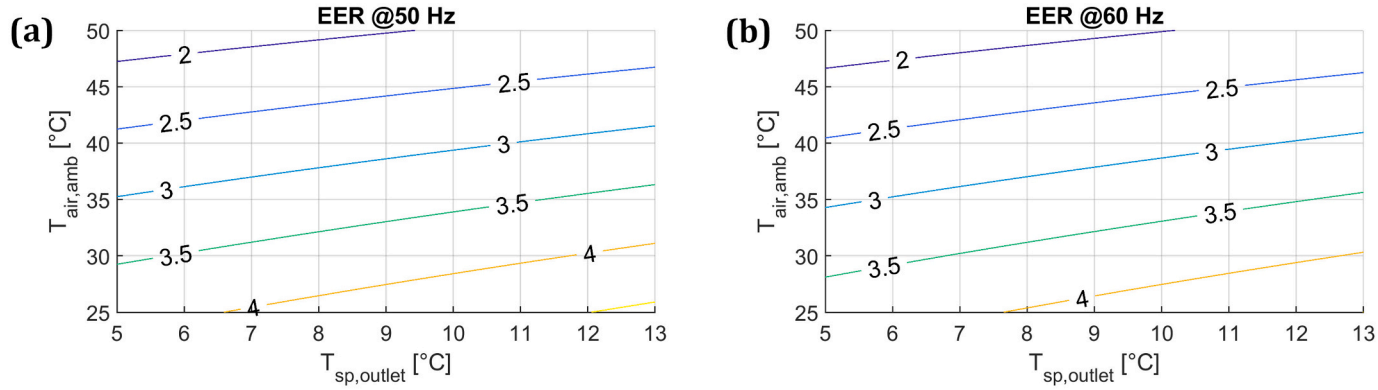

Fig. 8. Air-cooled chiller. **(a)** Energy Efficiency Ratio and **(b)** Fraction of EER at partial load.

Table 4
Nominal conditions for the heat exchangers sizing. $\dot{m}_c$, $T_{in,c}$, $\dot{m}_h$, $T_{in,h}$ are the mass-flow rates, and inlet temperatures at the cold and hot sides respectively.

	$\dot{m}_{hot}$ [kg.s^{-1}]	$\dot{m}_{cold}$ [kg.s^{-1}]	$T_{in,hot}$ [°C]	$T_{in,cold}$ [°C]	k [kW·K^{-1}]
HX_1	25.84	25.84	80	73	75.04
HX_2	9.50	9.50	60	30	154.47

All heat exchangers (HX) are in counterflow configuration and are sized for a temperature pinch of $\delta T = 2$ °C under the nominal conditions defined in Table 4. Note that to size HX_1, the inlet temperature in the cold side is estimated as:

$$T_{in,c} = T_6 = T_{GTH} - \frac{\dot{m}_{gen}}{\dot{m}_{GTH}}\delta T \tag{19}$$

The pressure drop of every fluid in the different heat exchangers (i.e. HX_1, HX_2, and the internal HXs of the absorption chiller) is assumed to be $\Delta\mathscr{P}_{HX} = 50$ kPa.

The pumps efficiency is assumed to be $\eta_{pump} = 0.75$. Therefore, the pumping power through one hydraulic element is calculated using Eq. *(20)*:

$$P_{pump} = \frac{\dot{m}\,\Delta\mathscr{P}}{\eta_{pump}\,\rho} \tag{20}$$

With ρ the water density. The electric power consumed by the pumps (P_1, P_2, P_3, P_4, P_5, P_6) are therefore:

$$\dot{W}^{el}_{P\_1} = \frac{\dot{m}_{gen}\left(\Delta\mathscr{P}_{6-4} + 2\Delta\mathscr{P}_{pipe}\right)}{\eta_{pump}\,\rho} = \frac{\dot{m}_{gen}\left(\Delta\mathscr{P}_{HX} + 2\Delta\mathscr{P}_{pipe}\right)}{\eta_{pump}\,\rho} \tag{21}$$

$$\dot{W}^{el}_{P\_2} = \frac{\dot{m}_{gen}\,\Delta\mathscr{P}_{14-15}}{\eta_{pump}\,\rho} = \frac{\dot{m}_{gen}\,\Delta\mathscr{P}_{HX}}{\eta_{pump}\,\rho} \tag{22}$$

$$\dot{W}^{el}_{P\_3} = \frac{\dot{m}_{to\ DHW}\,\Delta\mathscr{P}_{23-28}}{\eta_{pump}\,\rho} = \frac{\dot{m}_{to\ DHW}\,\Delta\mathscr{P}_{HX}}{\eta_{pump}\,\rho} \tag{23}$$

$$\dot{W}^{el}_{P\_4} = \frac{\dot{m}_{ev}\,\Delta\mathscr{P}_{37-30}}{\eta_{pump}\,\rho} = \frac{\dot{m}_{ev}\,\Delta\mathscr{P}_{HX}}{\eta_{pump}\,\rho} \tag{24}$$

$$\dot{W}^{el}_{P\_5} = \frac{\dot{m}_{to\ DHW}\,\Delta\mathscr{P}_{25-26}}{\eta_{pump}\,\rho} = \frac{\dot{m}_{to\ DHW}\,\Delta\mathscr{P}_{HX}}{\eta_{pump}\,\rho} \tag{25}$$

$$\dot{W}^{el}_{P\_6} = \frac{\dot{m}_{int}\,\Delta\mathscr{P}_{42-38}}{\eta_{pump}\,\rho} = \frac{\dot{m}_{int}\,\Delta\mathscr{P}_{HX}}{\eta_{pump}\,\rho} \tag{26}$$

The water viscosity is estimated in TRNSYS through the Pressure Drop Calculator (Type586) based on the fluid's temperature at each time step. Note that the consumption of P_7 is merged with the consumption of the ACC, and that the consumption of the cooling and DHW distribution pumps P_9 and P_10 are neglected. The overall electric power consumption $\dot{W}_{el}$ of the system is then:

$$\dot{W}_{el} = \sum_{i=0}^{8} \dot{W}^{el}_{P\_i} + \dot{W}^{el}_{sorp} + \dot{W}^{el}_{fan} + \dot{W}^{el}_{ACC} + \dot{Q}^{backup}_{DHW} \tag{27}$$

2.2.7. Control strategy

Four microprocessors control the system, each microprocessor controlling one or several actuators. Microprocessors #1, #2 and #4, which are modelled using Type2, perform a single comparison between two temperatures to execute a single operating mode labelled as 1 (in addition to a mode "0" that accounts for stand-by). Microprocessor #3, on the other hand, is modelled with a modified Type 40 [49] and performs 5 comparisons to determine 4 possible modes of operation (labelled from 1 to 4) in addition to a stand-by mode (labelled as 0).

Each comparator C compares an upper input temperature T_U to a lower one T_L. A lower dead band *ldb* and an upper one *udb* ensure hysteresis and prevent the controller from switching modes too often: If comparator C was previously true, C remains true if $(T_U - T_L) \geq ldb$ on the current time step but switches to false if $(T_U - T_L) < ldb$. Conversely, if comparator C was previously false, C remains false on the current time step if $(T_U - T_L) < udb$, but switches to true if $(T_U - T_L) \geq udb$. To foster the numerical convergence of the TRNSYS model, the input temperatures of all microprocessors are delayed by one time step before feeding the microprocessor.

Microprocessor #1 decides if geothermal energy must be brought to the system. To do so, it compares the geothermal temperature T_{GTH} with T_9 (the temperature at the top of Tank_1). It turns P_0 and P_1 on to feed Tank_1 when T_{GTH}-T_9 is greater than an upper dead band ($udb_1 = 3$ °C), and turns P_0 and P_1 off when the difference reaches a lower dead band ($ldb_1 = 2$ °C). The values of udb_1 and ldb_1 have been chosen to be in line with HX_1, which has been sized with a pinch of 2 °C (see section 2.2.6).

Microprocessor #2 decides if cooling from the ACC is needed (in case the absorption chiller is unable to meet the cooling needs). To do so, it compares the temperature at the bottom of the cooling tank Tank_5 (T_{40}) with the cooling setpoint temperature ($T_{sp\ cooling}$). It turns the ACC on when ($T_{40} - T_{sp\ cooling}$) is higher than udb_2, which is equal to −1 °C (i.e., when T_{40} is getting close to $T_{sp\ cooling}$), and stops the ACC when the difference reaches ldb_2, which is equal to −2 °C (i.e., when the tank has been sufficiently cooled down).

Microprocessor #3 decides if the absorption chiller must produce cooling and if DHW must be prepared (see Table 5). Four modes are possible: absorption chiller producing cooling (modes #1 and #2), production of DHW only, bypassing the generator of the absorption chiller (mode #3) and cooling and by-production of DHW with the outlet fluid from the generator (mode #4). To determine the mode, microprocessor #3 relies on 5 comparators:

Table 5
Characteristics of the microprocessor #3. "-1" means that the comparator plays no role in the selection of this mode

			Comparators					Outputs status		
			C1	C2	C3	C4	C5	chiller, P_4, P_6, div_3	P_3, P_5	P_2
	Upper input		T_{40}	32 °C	T_9	T_9	$T_{sp\ DHW}$			
	Lower output		$T_{sp,\ cooling}$	T_{36}	55 °C	T_{55}	T_{54}			
	Upper dead band [°C]		-1	0,25	0,25	3	−20			
	Lower dead band [°C]		−2	0	0	2	−18			
Mode	*1*	Absorption chiller produces cooling	1	1	1	−1	0	1	0	1
	2	Absorption chiller produces cooling	1	1	1	0	1	1	0	1
	3	DHW production	0	−1	−1	1	1	0	1	1
	4	Absorption chiller produces cooling, fluid leaving the generator is used for DHW production	1	1	1	1	1	1	1	1

- C1 compares T_{40} with $T_{sp\ cooling}$ to decide if cooling is needed, in the same way the comparator of microprocessor #2 does,
- C2 compares T_{36} (the temperature at the bottom of Tank_4) with 32 °C. According to manufacturer datasheets, 32 °C is the maximum recommended temperature at the intermediary source of the absorption chiller. Similarly, C3 compares T_9 (the temperature at the top of Tank_1) with 55 °C. C2 and C3 both enforces a tiny dead band of 0.25 °C. If C2 or C3 is false, then the absorption chiller is prevented to start.
- C4 compares T_9 (the temperature at the top of the geothermal tank Tank_1) with T_{55} (the temperature at the top of the DHW tank Tank_3) to determine if Tank_1 is hot enough to warm up the DHW tank. It is used to avoid heat being transferred back from the DHW tank to Tank_1. As for the single comparator of microprocessor #1 for HX_1, the upper and lower dead bands of C4 have been chosen to be in line with the pinch of HX_2.
- C5 compares $T_{sp\ DHW}$ (the DHW setpoint temperature) to T_{54} (the temperature at the top of the DHW tank Tank_3). It will be used to decide if DHW must be prepared. The upper dead band of −20 °C aims at maintaining T_{54} higher than $T_{sp\ DHW}$ by 20 °C, so that Tank_3 is always hot enough to provide DHW.

Microprocessor #3 starts the cooling production if C1, C2 and C3 are true, and:

- If C5 is false (mode 1): T_{54} is higher than $T_{sp\ DHW}$ by at least 20 °C, which means no DHW is immediately required and therefore, there is no reason to take the value of C4 into account.
- If C5 is true but C4 is false (mode 2): DHW is needed. However, given that T_9 is lower than the temperature at the top of the DHW tank (T_{55} + 2 °C), Tank_1 is too cold to warm Tank_3 up and therefore, no DHW is delivered.

Mode 3 (DHW production only) is selected if comparator C1 is false and both C4 and C5 are true, which means that the cooling tank is cold enough (no cooling is required immediately). C2 and C3 are not taken into account since the absorption chiller is not operated in this mode.

Mode 4 is for combined cooling and DHW production. All comparators must be true: cooling is needed (C1 is true), the operative conditions are in line with the absorption chiller specifications (C2 and C3 are true), the geothermal resource is warmer than the water in the DHW tank (C4 is true) and DHW is required (C5 is true).

Microprocessor #4 decides if the excess heat from the absorption chiller must be evacuated to the Cooling Tower. To do so, it compares T_{32} (the temperature at the top of Tank_4) with the wet bulb temperature of the air ($T_{wet\ bulb}$). It starts the CT when the temperature at the top of the CT tank (T_{32}) is higher than ($T_{wet\ bulb} + udb_{4,1}$), with $udb_{4,1} = 5$ °C, and stops the CT when T_{32} falls to ($T_{wet\ bulb} + ldb_{4,1}$), with $ldb_{4,1} = 4.5$ °C. The water is therefore injected into the CT at a temperature above the desired outlet temperature ($T_{sp}^{CT} = T_{wet\ bulb} + dT_{sp}^{CT}$), where dT_{sp}^{CT} is the CT approach set fixed to 3 °C (see §2.2.4).

The set points of the outlet temperature from the absorption chiller and the air-cooled chiller are respectively $T_{38} = T_{sp\ cooling} - dT_{sp}^{sorp}$ and $T_{45} = T_{sp\ cooling} - dT_{sp}^{ASHP}$ with $dT_{sp}^{sorp} = dT_{sp}^{ASHP} = 1$ °C. This ensures the cooling tank is always cold enough when cooling is required.

The valves mix_4 and div_4 ensure that the distributed DHW temperature (point 59) does not overreach $T_{sp\ DHW}$, redirecting some tap water into the distribution loop if needed (point 62) rather than towards the DHW tank (point 63). Similarly, mix_2 and div_2 prevents entering the load side of HX_2 (point 25) with a temperature higher than 80 °C. mix_5 and div_5 prevent sending undercooled water into the cooling loop (point 47) by redirecting some warmed water flowing back from the building (point 49). P_9 is operated so that $T_{48} - T_{47} = 12–7$ °C = 5 °C, therefore $\dot{m}_{cooling} = \frac{\dot{Q}_{cooling}}{C_p(T_{48}-T_{47})}$.

2.3. Key Performance Indicators (KPI)

Throughout the paper, two key indicators will be used for both economic and environmental assessment. The first KPI is the normalized electric consumption of the system W_{el}^{*}:

$$W_{el}^{*} = \frac{W_{el}}{Q_{demand}} = \frac{W_{el}}{Q_{cooling} + Q_{DHW}} \tag{28}$$

Another important indicator is $Q_{sorp}^{ev\ \sim}$, the normalized amount of cooling produced by the absorption chiller relative to the total cooling load only:

$$Q_{sorp}^{ev\ \sim} = \frac{Q_{sorp}^{ev}}{Q_{cooling}} \tag{29}$$

Note that the exergy destruction rate is not analyzed in this paper.

3. Results

3.1. Preliminary sizing

For the preliminary sizing defined in Table 2, most of the cooling requirement is covered by the absorption chiller (see Fig. 9a). The yearly electricity consumption of the system is $W_{el} = 76.6$ MWh.y^{-1} or $W_{el}^{*} = 76.6/(570.5 + 151.9) = 0.106$. The three main electricity consumers are the ACC, followed by the CT fans and the pump P_4 (see Fig. 9b). The absorption chiller delivers $Q_{sorp}^{ev\ \sim} = 0.817$ on an annual basis. Note that the entire DHW need is covered by the geothermal fluid without any backup.

During the wet season (July to November), the simultaneous increase in the cooling demand and the wet bulb temperature decreases the capacity of the absorption chiller during daytime, leading to an overall increase of the ACC contribution (see Fig. 9c and d). This is illustrated by Fig. 10: the absorption chiller is constantly operated (microprocessor #3 in mode #1) with sporadic by-production of DHW when microprocessor

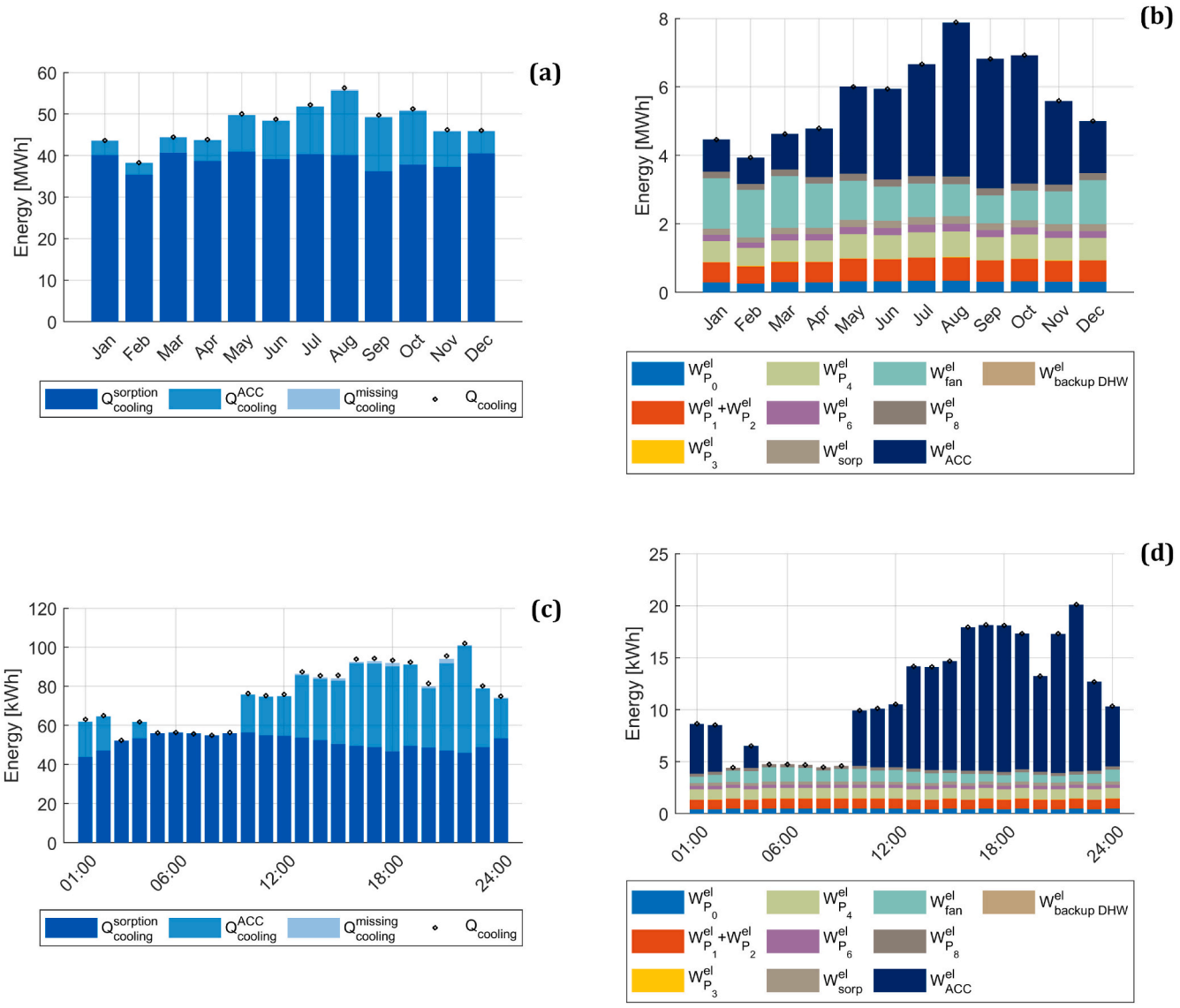

Fig. 9. Cooling sources and electricity consumption (a, b) on a monthly basis and (c, d) on an hourly basis for the 2nd of September 2050. Preliminary sizing defined in Table 2.

#3 switches to mode #4. Microprocessors #1 and #4 follow microprocessor #3 by operating P_0, P_1 and the CT. From approximatively 8:00 to 22:00, the absorption chiller is not able to maintain the bottom of the cooling tank (point 38 in Fig. 3) to the cooling set point (7 °C, see Fig. 10d), which makes the ACC to operate so that the cooling setpoint is maintained. Note that, for this rather unfavorable day, the maximum inlet intermediate temperature in the absorption chiller is 29.8 °C, while the mains water is about 32 °C. Therefore, in the studied case, the CT is systematically a better heat sink for the absorption chiller than the mains water. However, in milder climates with cooler mains water, the excess heat from the condenser and absorber of the absorption chiller could be used to pre-heat the mains water without a negative impact on the absorption chiller efficiency.

3.2. "Status quo" scenario

A "Status quo" will serve as a comparison with the geothermal absorption chiller. It is basically an ACC with a fuel boiler for DHW, as it is common in the French overseas. This system has been modelled by setting negligible values for $\dot{Q}_{sorp}^{ev}$ and $\dot{m}_{GTH}$. All cooling is delivered by the ACC (i.e. $Q_{sorp}^{ev\ \sim} = 0$). The electricity consumption is entirely tracked back to the ACC operation with W_{el} = 164.9 MWh.y^{-1} or $W_{el}^{\sim} = W_{el}/Q_{cooling}$ = 0.228. In other words, the Seasonal Performance Factor of the ACC over a whole year would be SPF ≈ 1/0.228 ≈ 4.39. The maximum thermal power provided by the DHW boiler is $\dot{Q}_{DHW}^{max}$ = 28.3 kW.

3.3. Sensitivity analysis around the preliminary sizing

A sensitivity analysis of $Q_{sorp}^{ev\ \sim}$ and W_{el}^{*} around the preliminary sizing was carried out, considering the TRNSYS parameters reported in Table 2 as variable. This enlightens the following trends:

- *Geothermal resource* (see Fig. 11): $Q_{sorp}^{ev\ \sim}$ increases with the geothermal temperature T_{GTH} or flow rate $\dot{m}_{GTH}$. As explained in §2.2.1, a geothermal resource with a much lower available flow rate may only slightly affect the cooling delivered by the absorption chiller (e.g. for T_{GTH}=80 °C, $Q_{sorp}^{ev\ \sim} \approx 0.73$ for $\dot{m}_{GTH} = 0.5\,\dot{m}_{gen}$ instead of $Q_{sorp}^{ev\ \sim} \approx 0.82$ for $\dot{m}_{GTH} = \dot{m}_{gen}$). Reversely, only a fraction of the geothermal flow rate considered in the preliminary sizing is

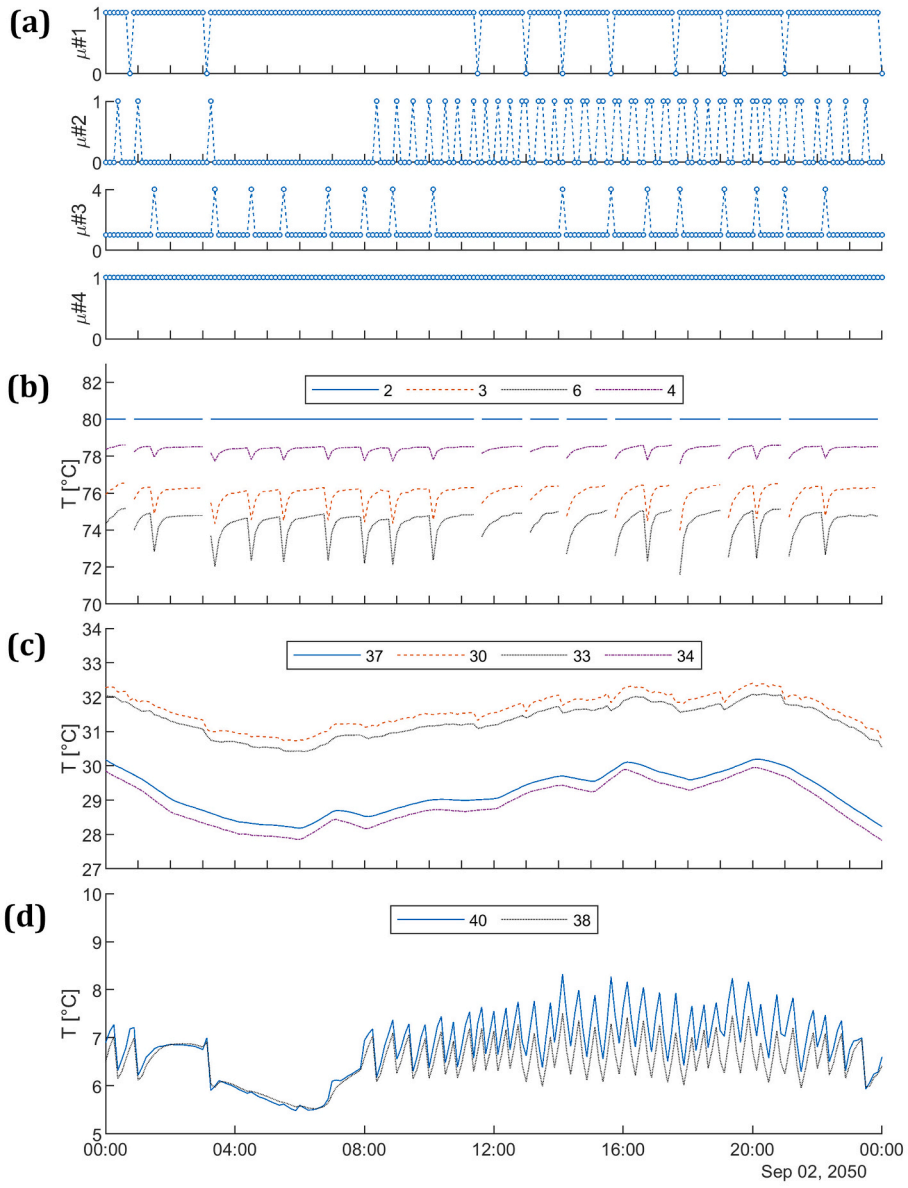

Fig. 10. Evolution of several variables with time for September 2, 2050. (a) Microprocessors' operating modes; (b) inlet and outlet temperatures of the fluids in the geothermal HX (HX_1), (c) absorption chiller's heat sink heat transfer fluid temperature at the inlet and outlet of the chiller and of the CT, and (d) chilled water temperature at the absorption chiller's outlet and at the bottom of the cold storage tank. Preliminary sizing defined in Table 2.

necessary to power the absorption chiller if the temperature is higher than 80 °C.

- *Thermal demand and distribution* (see Fig. 12a-d): The maximum cooling power $\dot{Q}^{max}_{cooling}$ has a limited effect since all machines (absorption chiller, ACC, cooling tower) behave the same, no matter their nominal capacity. Increasing the cooling setpoint temperature $T_{sp\ cooling}$ [°C] significantly increases the cooling delivered the by absorption chiller and consequently decreases the use of the ACC. A larger Tank_5 allows the storage of chilled water produced by the absorption chiller under favorable conditions (e.g., low wet bulb temperature early in the morning, see parameter Δt_5). Decreasing the fraction of DHW r_{DHW} (where $r_{DHW} = 0$ if there is no DHW demand and $r_{DHW} = 1$ if DHW is computed according to §2.1.2) increases W^*_{el} as it removes the "free" heat from the generator outlet used for DHW preparation.
- *Absorption chiller* (see Fig. 12e): The delivered cooling increases with the nominal cooling power. For instance, $Q^{ev}_{sorp}{}^{\sim}$ reaches 0.91 for a chiller whose nominal power $\dot{Q}^{ev}_{sorp}$ equals twice the cooling demand $\dot{Q}^{max}_{cooling}$.
- *Cooling tower* (see Fig. 12f-i): The exponent n in Merkel's correlation has little influence upon $Q^{ev}_{sorp}{}^{\sim}$ and W^*_{el} contrarily to the exchange coefficient c, as reported in [37,38]. Electric consumption can be slightly decreased if the CT water flow rate is slightly higher than the absorption chiller intermediary flow rate ($\dot{m}_{int} \approx 1.2\ \dot{m}_{w,CT}$). A larger CT with a much higher air flow rate than water flow rate (e.g. $\dot{m}^{max}_{air,CT} \approx 3\ \dot{m}_{w,CT}$) achieves a much lower electric consumption, since fans operate at lower speed on a more regular basis.
- *Control* (*see* Fig. 12j-n): Setting a low algebraic value to udb_2 causes the ACC to start more often, decreasing the operation range of the absorption chiller and increasing the overall electric consumption. Increasing udb_1 causes Tank_1 to be warmed up by the geothermal fluid on a less regular basis, decreasing the overall system efficiency, while $udb_{4,1}$ plays little role. For the preliminary sizing, a CT approach $dT^{CT}_{sp} \approx 3$ °C seems to be optimal, since a lower value causes

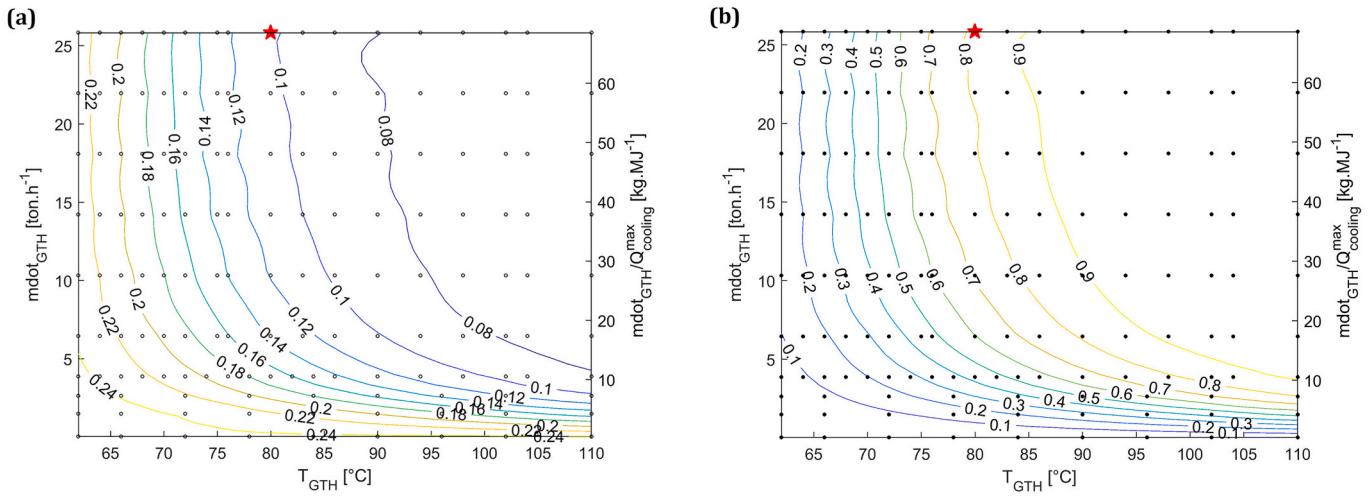

Fig. 11. (a) Share of cooling from the absorption chiller $Q_{sorp}^{ev}{}^{\sim}$; (b) Normalized electricity $W_{el}^{*}=W_{el}/Q_{demand}$ as a function of geothermal temperature T_{GTH} and flow rate $\dot{m}_{GTH}$. The TRNSYS results are represented with black dots. The red star accounts for the preliminary sizing defined in Table 2. (For interpretation of the references to colour in this figure legend, the reader is referred to the web version of this article.)

the CT to run on a much more regular basis which increases the electric fan and overall consumption, though the absorption chiller delivers more cooling. Beyond this point, the CT ability to lower the intermediary temperature decreases, resulting in more cooling provided from the ACC instead of the absorption chiller.

- *Buried twin pipes* (see Fig. 12o-q): Longer buried pipes results in increased electric consumption of P_1 and the overall system, though it may be mitigated by decreasing the nominal pressure loss $\Delta_{\prime\prime}$ and increasing of the pipes diameter. Slightly increasing the normalized casing diameter $d_{casing}{}^{*}$ improves the insulation and decreases the heat loss along the pipes, resulting in hotter fluid delivered to the absorption chiller which, in turns, produces more cooling.

4. Discussion: System optimization

The sensitivity analysis shows that the 19 investigated parameters have an impact upon both $W_{el}{}^{*}$ and $Q_{sorp}^{ev}{}^{\sim}$ KPIs, though to different extents. The preliminary sizing introduced in Table 2 is devoted to illustrate the system behavior but might be far away from a technical and economic optima. Leaving apart the CT mass transfer constant and exponent left to $c = 1.3$ and $n = 0.6$ respectively, the combination of 17 parameters must be investigated to determine optima. If one wants to explore the effect of 3 values per parameter, then the overall number of TRNSYS simulations would be $3^{17} \approx 129 \times 10^{6}$, an unrealistic high value. To overcome this, one needs to build fast-to-run approximations of $W_{el}{}^{*}$ and $Q_{sorp}^{ev}{}^{\sim}$, also known as *surrogates*, through a statistical analysis of a limited number of TRNSYS simulations, and then use these surrogates in the optimization process. Surrogate modelling applied to energy in buildings has been a booming research domain for the past few years (see for example [50] for a comprehensive overview of challenges, techniques, applications and past successes).

4.1. Framework for multi-objective optimization

4.1.1. Surrogate modelling of $W_{el}{}^{*}$ and $Q_{sorp}^{ev}{}^{\sim}$

The $D = 17$ parameters and their bounds are reported in Table 7. The problem is expressed as a function of a single extensive parameter ($\dot{Q}_{cooling}^{max}$) and a set of intensive parameters. Extensive parameters ($\dot{m}_{GTH}$, $\dot{m}_{air,CT}^{max}$, $\dot{m}_{w,CT}$, L) have been replaced with the intensive quantities $\dot{m}_{GTH}/\dot{Q}_{cooling}^{max}$, $\dot{m}_{air,CT}^{max}/\dot{m}_{w,CT}$, $\dot{m}_{w,CT}/\dot{m}_{int}$ and $q_{\ell}{}^{-1} = L/\left(5500 \bullet \dot{Q}_{cooling}^{max}\right)$ respectively. Each model parameter x_i ($i \leq 1 \leq D$) is transformed into χ_i, a variable normalized in the range [0;1] (see Table 7) though linear (Eq. (30)) or concave transformations (Eq. (31)):

$$\chi_i = \frac{x_i - x_{i-}}{x_{i+} - x_{i-}} \tag{30}$$

$$\chi_i = 0.5\left(\frac{x_i - x_{i-}}{x_{i+} - x_{i-}}\right) + 0.5\left(\frac{x_i{}^{0.25} - x_{i-}{}^{0.25}}{x_{i+}{}^{0.25} - x_{i-}{}^{0.25}}\right) \tag{31}$$

The concave transformation ensures a higher sampling density close to the lower bound x_{i-} and was preferentially used for the variables changing by at least one order of magnitude.

The authors have chosen regression through Gaussian Processes (GP), sometimes referred to as kriging, for its flexibility [51]. A GP is a non-parametric regression (or machine learning) technique, which means it does not rely on any a priori restrictive assumption about the structure of the function, such as a "linear" or "quadratic" regression. The GP "learns" the underlying structure of the data to make predictions. Though GP techniques have been developed for high dimensional datasets [52–54], standard GPs with constant basis (i.e. simple kriging) and Matérn3/2 kernels have been used for this work. One advantage of GP is their interpretability (see Appendix A for theoretical background and further discussion).

The quality of the surrogate is estimated through cross-validation [55], a procedure where a part $1/n$ of the data is randomly selected and left apart (here $n = 5$), acting as a test sample. A surrogate is fitted on a fraction $(1–1/n)$ of the sample and the procedure is repeated n times by permuting the samples. The metric for the estimation of the quality of the surrogate of an output f is the Root Mean Square Error (RMSE), defined by Eq. *(32)*:

$$RMSE(f) = \left(\sum_{i=1}^{N} \frac{\left[(f)_{TRNSYS} - (f)_{surrogate}\right]^2}{N}\right)^{1/2} \tag{32}$$

The surrogates of both KPI are built through the iterative generation of points χ ($\chi \in [0;1]^D$) and subsequent evaluation of TRNSYS models, starting with $N = 170$ points at the first iteration. The points are generated with a Latin Hyper Square (LHS), a method with enhanced space filling properties [56]. They must fulfil the constraint (C1) to ensure that the heat evacuation to the CT is started only when the wet bulb temperature is above the CT approach by 1 °C (Eq. *(33)*).

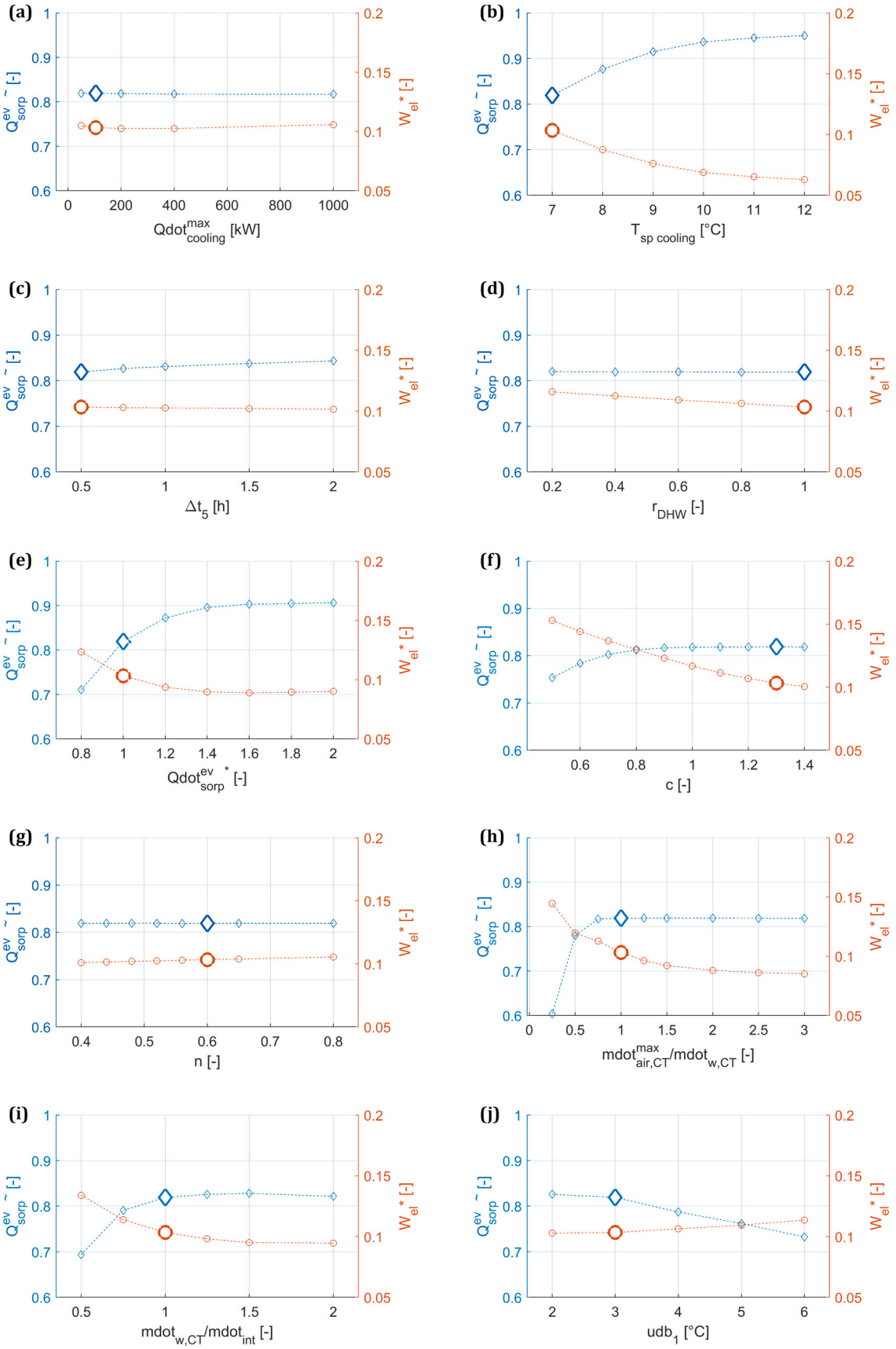

Fig. 12. One-at-a-time sensitivity analysis. The bolder points account for the preliminary sizing defined in Table 2. Thermal demand and distribution: (a) Maximum cooling power $\dot{Q}^{max}_{cooling}$; (b) Cooling set point temperature $T_{sp\ cooling}$; (c) Nominal storage duration of cooling tank Δt_5 [h]; (d) Fraction of DHW r_{DHW}. Absorption chiller: (e) Normalized nominal cooling power $\dot{Q}^{ev\ *}_{sorp}$. Cooling Tower: (f) Coefficient c; (g) Exponent n; (h) Ratio of maximal air flow rate to water flow rate

$\dot{m}^{max}_{air,CT}/\dot{m}_{w,CT}$; (i) Ratio of CT water flow rate to the intermediary flow rate of the absorption chiller $\dot{m}_{w,CT}/\dot{m}_{int}$. Control strategy: (j) Upper dead band of microprocessor #1 udb_1; (k) Upper dead band of microprocessor #2 udb_2; (l) Upper dead band of comparator C1 of microprocessor #4 $udb_{4,1}$; (m) Difference between the cooling setpoint and the absorption chiller outlet temperature dT^{sorp}_{sp}; (n) Cooling tower approach dT^{CT}_{sp}; Buried pipes: (o) Pipe length; (p) Normalized casing diameter d_{casing}* (L = 500 m); (q) Nominal linear pressure drop $\Delta_{/}$ (L = 500 m).

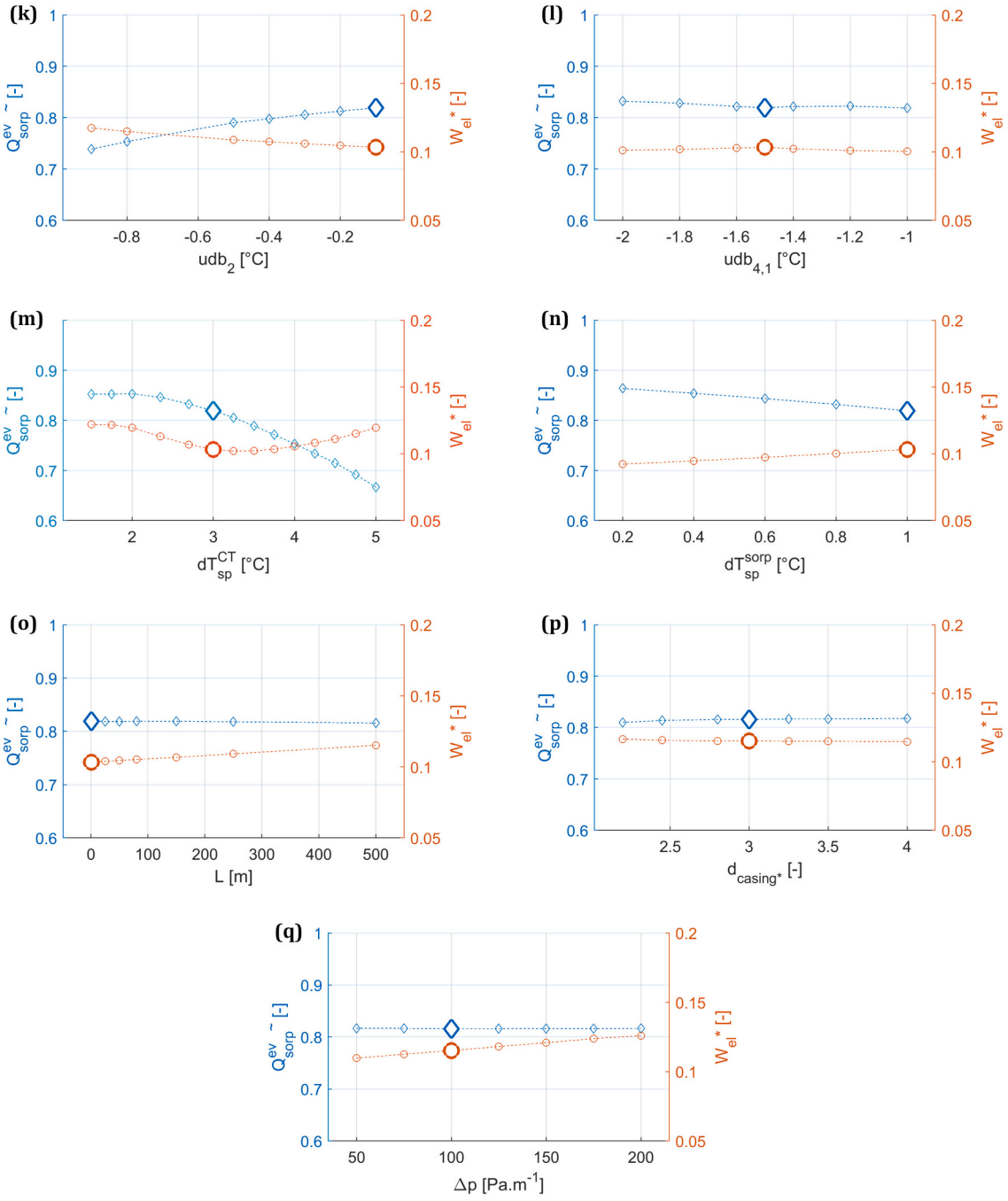

Fig. 12. (*continued*).

$$(C1): udb_{4,1} \geq dT_{sp,CT} + 1^{\circ}C \tag{33}$$

During the following iterations, a second constraint (C2) excludes the configurations with excessive electric consumption since they would be of no interest compared to the *status quo* (Eq. (34)):

$$(C2): W_{el}^{*}(\chi) < 0.3 \tag{34}$$

The refinement is stopped when $N = 4589$ TRNSYS models have been evaluated since a negligible improvement of the RMSE of W_{el}* GP is observed (see Fig. 13a). The RMSE of W_{el}* reaches 0.0115 and the GP is in good agreement with the TRNSYS models outputs (see Fig. 13b). For 75 points on Pareto fronts reported in section 4, the RMSE of W_{el}* is equal to 0.116. As these points have not been used for the GP training, the similarity of both RMSE indicates the robustness of the surrogate. Note that a quadratic regression summing a constant term and all linear, quadratic and interactions terms (respectively χ_i, χ_i^2 and $\chi_i \bullet \chi_j$ with $i \neq j$) has an RMSE equal to 0.0274. In other words, the GP outperforms the quadratic regression when learning the underlying structure of the data.

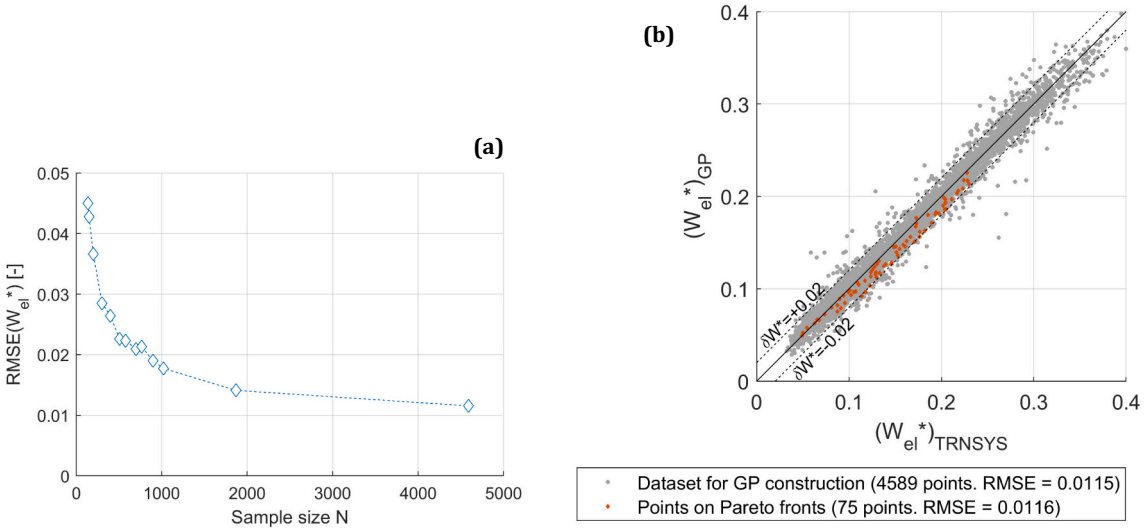

Fig. 13. (a) Evolution of the RMSE during the construction of W_{el}* surrogate. (b) Quality of this surrogate: TRNSYS data vs GP predictions, for the datasets used for learning and for results of the optimization reported in §4 (three points per scenario: one trade-off and the two ends of each Pareto front). The dotted black lines $\delta W = \pm 0.02$ indicate an absolute error of ± 0.02 on the prediction of W_{el}*.

Table 6
Cost and GWP of energies.

Energy	Cost at year 1 as a function of delivered energy E [€.MWh^{-1}] [a]	Yearly increase [%.y^{-1}]	GWP [kgCO$_2$eq.MWh^{-1}] [b]
Heating Oil	$110.3 - \frac{87.8}{1 + exp\left(25.43 - 16.62log_{10}(E) + 3.79\,(log_{10}(E))^2 - 0.306(log_{10}(E))^3\right)}$	0.90	321
Electricity	$192.5 - \frac{135.3}{1 + exp\left(13.72 - 11.8log_{10}(E) + 3.32\,(log_{10}(E))^2 - 0.325(log_{10}(E))^3\right)}$	1.20	840

[a] Adapted from data provided by the French Ministry of Ecology and Sustainable Development [57,58]
[b] According to Base Carbone by French Energy Agency ADEME [62]. The electricity GWP is from Martinique.

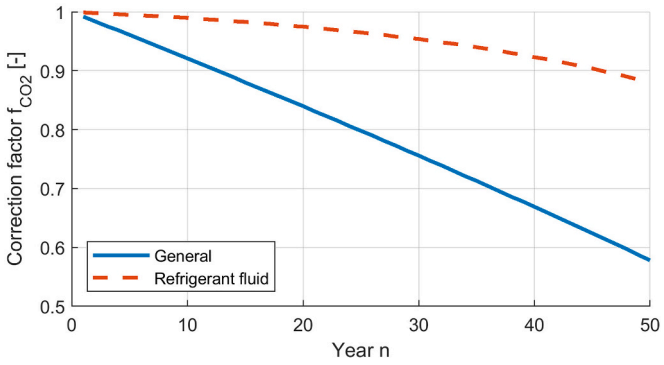

Fig. 14. Correction factor $f_{CO2}(n)$ according to the French thermal regulation RE2020 for the general case and the specific case of a refrigerant fluid.

4.1.2. Definition of the optimization problem

Multi-objective optimization aims at finding all possible designs when two or more competing objectives are considered. The resulting set of designs is known as the *Pareto front*. No design points can be more favorable than the *Pareto front*: an improvement in one objective requires a degradation in all other objectives.

4.1.2.1. Objectives. The authors have considered the minimization of two objectives:

- the cost of energy c (see Eq. (35)) expressed in €.MWh^{-1} and computed on $N_{y,LCOE} = 25$ years,
- the Global Warming Potential (GWP) γ (see Eq. (36)) of the energy, expressed in kgCO$_2$eq.MWh^{-1}.

$$c = \frac{1}{N_{y,LCOE} \cdot Q_{demand}} \left(C_0 + \sum_{n=1}^{N_{y,LCOE}} \sum_{i=1}^{N_{expense}} C_{1,i} \left(\frac{1+\alpha_i}{1+a} \right)^n \right) \quad (35)$$

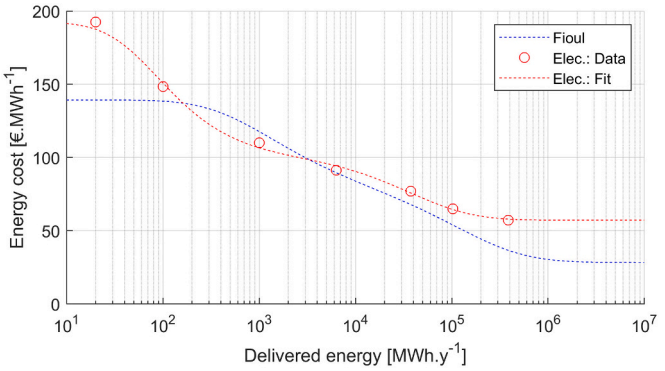

Fig. 15. Cost of energy as a function of the delivered energy. Adapted from data provided by the French Ministry of Ecology and Sustainable Development [57,58].

component making, distribution, installation, maintenance and end of life) and $\gamma_{e,i}$ is the GWP associated with energy i. According to the French environmental regulation of buildings RE2020 [59], the GWP is computed over $N_{y,GWP} = 50$ years, and the GWP at year n is corrected by a function $f_{CO2}(n)$ (see Fig. 14). Discussing the relevance of the RE2020 framework is beyond the scope of this paper. Note that compared with continental France, the electricity GWP in French overseas is extremely high (here 840 vs. 79 kgCO2eq.MWh^{-1}) since electricity is mostly produced by fossil fuels combustion. The GWP of the oil boiler and air-cooled chiller are computed according to datasheets integrated in the RE2020 framework, while the GWP of the absorption chiller and Cooling Tower are derived from already published papers (see Table 8).

The electric consumption W_{el} is estimated from the surrogate as $W_{el}(\chi) = W_{el}^{*}(\chi) \times Q_{demand}\left(\dot{Q}_{cooling}^{max}, r_{DHW}\right)$ where $Q_{demand}\left(\dot{Q}_{cooling}^{max}, r_{DHW}\right)$ [MWh.y^{-1}] is a simple quadratic regression (with coefficient of determination $R^2 \approx 1$):

$$Q_{demand}\left(\dot{Q}_{cooling}^{max}, r_{DHW}\right) = \left(16.018 + 66.999 \bullet \dot{Q}_{cooling}^{max} + 1.6057 \bullet r_{DHW} + 4.5835 \bullet \dot{Q}_{cooling}^{max} \bullet r_{DHW} - 9.1558 \bullet \dot{Q}_{cooling}^{max\ 2} - 0.19682 \bullet r_{DHW}^{2}\right)^2 \quad (37)$$

$$\gamma = \frac{1}{N_{y,GWP} \cdot Q_{demand}} \sum_{n=1}^{N_{y,GWP}} \left(\sum_{i=1}^{N_{comp}} \Gamma_{comp,i} f_{CO2}(n) + \sum_{i=1}^{N_{energ}} \gamma_{e,i} E_i f_{CO2}(n) \right) \quad (36)$$

In Eq. (35), C_0 is the initial investment, $C_{1,i}$ is the cost of expense i at year 1, α_i is the yearly increase of this expense i (in %.y^{-1}), and a is the discount rate, assumed to be 3.55%.y^{-1} (see Table 6). Furthermore, the maintenance cost is assumed to increase by 1.41% per year, and the assumptions regarding the cost and CO_2 content of oil and electricity are reported in Table 6 and Fig. 15. Note that the refurbishment of the tanks, absorption chiller, air-cooled chiller, and gas boiler is included in the cost, since their lifetime (20–22 years) is less than $N_{y,LCOE}$. The costs of energy (electricity and oil) are estimated based on a survey published by the French Ministry of Ecology and Sustainable Development on a yearly basis [57,58]. The evolution of the macroeconomic parameters (inflation, discount rate, electricity and oil costs) are in line with the the French subsidy fund *Fonds Chaleur Renouvelable*. Discussing the relevance of the values of the macroeconomic parameters and their evolutions over 25 years is beyond the scope of this paper. The investment and maintenance costs of every component are derived from already published regressions or are established from datasets (see Table 8).

In eq. (36), $\Gamma_{comp,i}$ is the GWP of component i (including the

4.1.2.2. Bounds and constraints. χ_i must be in the range [0;1]^D. The constraint (C1) applies.

4.1.2.3. Numerical resolution. The multi-objective optimization problem was solved using Matlab. As recommended by Matlab developers, the Pareto front is determined through a two-steps procedure with first an exploration of the design space by a global optimizer (*paretosearch* function) followed by a refinement with a local optimizer (*fgoalattain* function) [60,61]. Conventionally, a trade-off between the competing objectives is defined as the closest point to the unachievable simultaneous minimization of both cost c and GWP γ. This point on the Pareto front $c(\gamma)$ minimizes the dimensionless distance $\ell = \sqrt{\left(\frac{c(\gamma)-min(c)}{min(c)}\right)^2 + \left(\frac{\gamma-min(\gamma)}{min(\gamma)}\right)^2}$:

$$\{c,\gamma\}_{tradeoff} = min\left(\sqrt{\left(\frac{c(\gamma)-min(c)}{min(c)}\right)^2 + \left(\frac{\gamma-min(\gamma)}{min(\gamma)}\right)^2}\right) \quad (38)$$

4.2. Optimization of a baseline configuration

The configuration to be optimized is described in Table 7. The value of the fixed parameters reported in Table 7 are identical to the

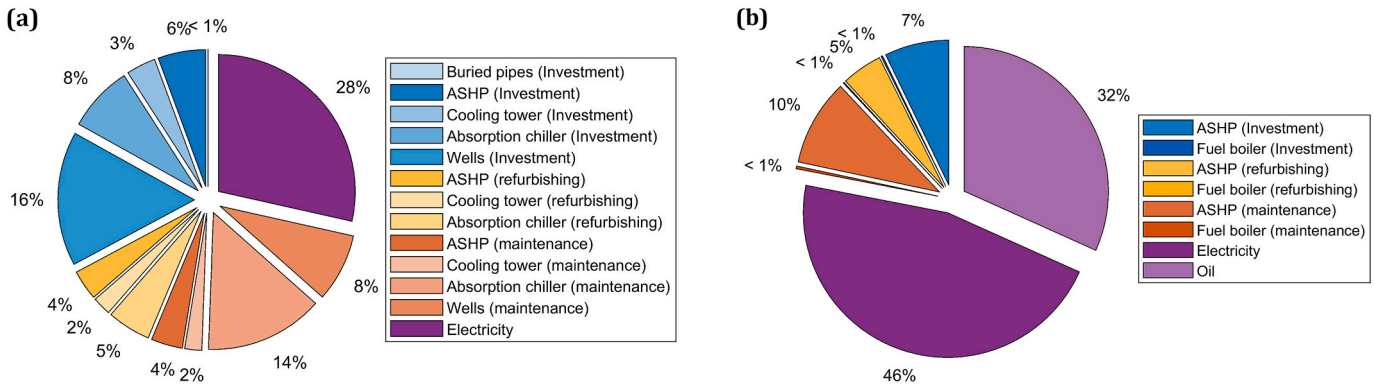

Fig. 16. Comparison of the structures of the cost c for **(a)** the tradeoff (baseline optimization) and **(b)** the status quo.

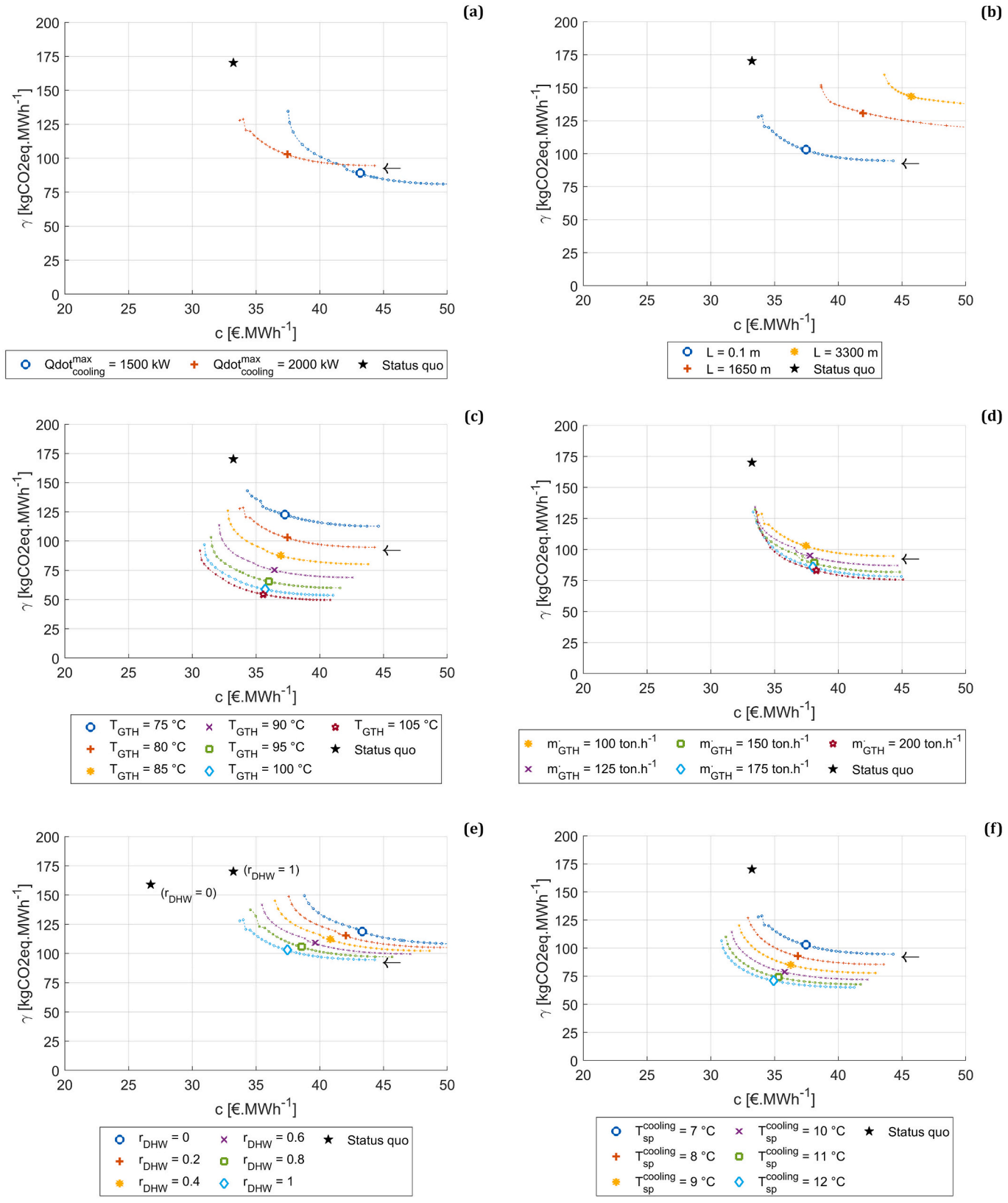

Fig. 17. *Influence of some parameters upon the Pareto front: (a) maximum cooling power* $\dot{Q}^{max}_{cooling}$; (b) buried pipe length L; (c) geothermal temperature T_{GTH}; (d) geothermal flow-rate $\dot{m}_{GTH}$; (e) ratio of DHW r_{DHW}; (f) and cooling set point temperature $T_{sp\ cooling}$. The trade-off is highlighted and the black arrows indicate the reference scenario defined in Table 7.

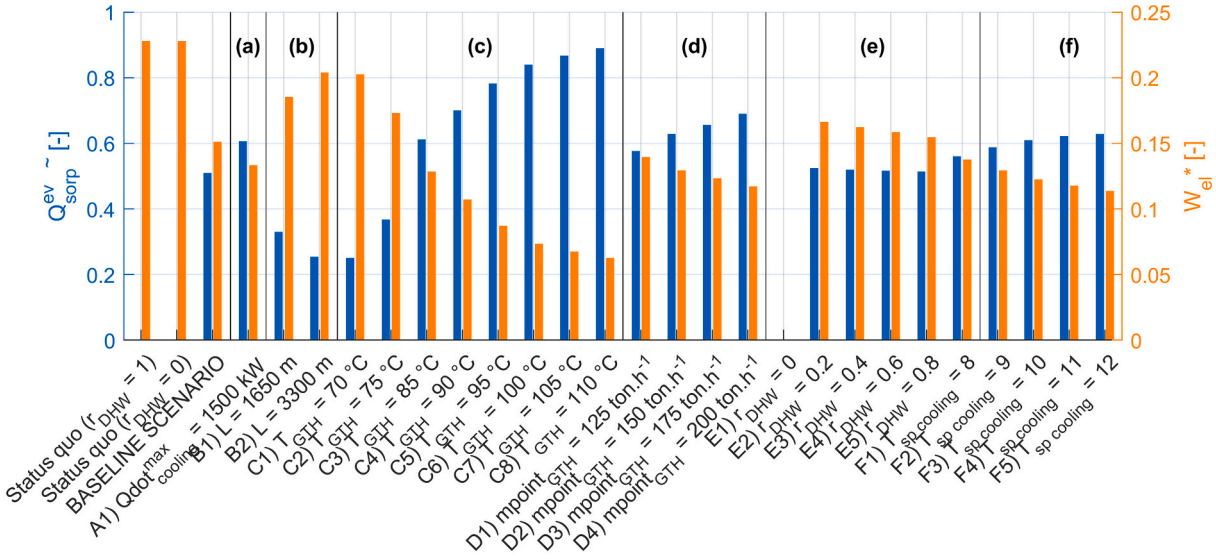

Fig. 18. Normalized share of cooling from the sorption chiller $Q^{ev}_{sorp}{}^{\sim}$ and electricity consumption $W_{el}{}^{*}$ for the trade-offs reported in Fig. 17, as re-computed by TRNYS. The bold lowercase letters refer to the subplots in Fig. 17. The TRNSYS computation for $r_{DHW} = 0$ did not converge and is not represented.

Table 7
TRNSYS parameters explored for the construction of the surrogates (D = 17 variables)

Component	TRNSYS parameters (Predictor variables of the surrogates)	Lower bound	Upper bound	Transform	Value used for the optimization reported in § 4.2 [a]
Thermal demand and distribution	Maximum cooling power $\dot{Q}^{max}_{cooling}$ [kW]	50	2000	Concave	2000
	Cooling set point temperature $T_{sp\ cooling}$ [°C]	7	12	Linear	7
	Nominal storage duration of cooling tank Δt_5 [h]	0.25	3.0	Concave	
	Fraction of DHW r_{DHW} [−] (= 0 if no DHW; = 1 if DHW computed in §2.1.2; varies linearly between bounds)	0	1	Linear	1
Geothermal resource	Geothermal temperature T_{GTH} [°C]	60	110	Concave	80
	Specific mass flow rate $\dot{m}_{GTH}/\dot{Q}^{max}_{cooling}$ [kg.MJ^{-1}]	1	100	Concave	13.9 [b]
Absorption chiller	Normalized nominal cooling power $\dot{Q}^{ev}_{sorp}{}^{*} = \frac{\dot{Q}^{ev}_{sorp}}{\dot{Q}^{max}_{cooling}}$ [−]	0.25	2.0	Concave	
Cooling tower	Ratio of maximal air flow rate to water flow rate $\dot{m}^{max}_{air,CT}/\dot{m}_{w,CT}$ [−]	0.5	3.0	Linear	
	Ratio of the CT water flow rate to the intermediary flow rate of the absorption chiller to $\dot{m}_{w,CT}/\dot{m}_{int}$	0.5	2.0	Linear	
Control	Upper dead band of microprocessor #2 udb_2 [°C]	−1.2	−0.5	Linear	
	Upper dead band of microprocessor #1 udb_1 [°C]	3	7	Linear	
	Difference between the cooling setpoint and the absorption chiller outlet temperature dT^{sorp}_{sp} [°C]	0	2	Linear	
	Cooling tower approach dT^{CT}_{sp} [°C]	2	4	Linear	
	Upper dead band of comparator C1 of microprocessor #4 $udb_{4,1}$ [°C]	3	6	Linear	
Buried twin pipes	Pipe length per estimated delivered energy $q_\ell{}^{-1} = L/\left(5500 \bullet \dot{Q}^{max}_{cooling}\right)$ [m.MWh^{-1}] [c]	0	1	Linear	0
	Normalized casing diameter d_{casing}* [−]	2.5	5	Linear	2.5 [d]
	Nominal linear pressure drop $\Delta_{\mathscr{P}}$ [Pa.m^{-1}]	50	200	Linear	100 [d]

[a] Empty elements indicates the design variables to be optimized.
[b] $\dot{m}_{GTH} = 100 \times 10^3$ kg.h^{-1}
[c] District Heating Networks are often considered too expensive if the delivered energy density is below 1 MWh.m^{-1}. t_{eq} = 5500 h is the cooling duration at full cooling load.
[d] Fixed if the pipe length L is zero, left to the optimizer otherwise.

preliminary sizing values reported in Table 2, except the much higher maximum cooling power $\dot{Q}^{max}_{cooling}$ (2 MW instead 104.3 kW) and the lower specific geothermal flow rate of $\dot{m}_{GTH}/\dot{Q}^{max}_{cooling} = 13.9$ kg.MJ^{-1} (i.e. $\dot{m}_{GTH} = 100$ ton.h^{-1}).

The cost c and GWP γ at the trade-off are 37.5 €.MWh^{-1} and 103.1 kgCO$_2$eq.MWh^{-1}, and 33.2 €.MWh^{-1} and 170.1 kgCO$_2$eq.MWh^{-1} for the *status quo* scenario. The Appendix C reports the values of the design variables at the trade-off. Though the nominal cooling power $\dot{Q}^{ev}_{sorp}$ equals 2.0 × 0.77 = 1.54 MW, the absorption chiller covers only $\dot{Q}^{ev}_{sorp}{}^{\sim} = 0.56$ of the cooling load. An alternative design focusing on the GWP minimization leads to $\gamma = 94.7$ kgCO$_2$eq.MWh^{-1} at the expense of a higher cost ($c = 44.3$ €.MWh^{-1}), as represented by the far right end of the Pareto fronts in Fig. 17. The larger absorption chiller ($\dot{Q}^{ev}_{sorp} = 2.29$ MW) provides then more cooling ($\dot{Q}^{ev}_{sorp}{}^{\sim} = 0.70$).

The initial investment represents about one third of the total cost, so does the energy cost and the maintenance and refurbishment altogether (see Fig. 16a). The energy cost accounts for 78% of the total cost of the status quo, which exposes the *status quo* installation to the volatility of

Table 8
Assumption related to cost and GWP of each system component. All powers are expressed in kW

	Cost C [€]		Global Warming Potential Γ [kgCO2eq]	
Component	Investment	Maintenance	Fabrication, installation, use (excluding energy) and dismantling	Lifetime [years]
Oil boiler	$C_0 = 2500 + 5000 \bullet \left(1 - exp\left(-0.01381 \bullet \dot{Q}_{DHW}^{max}\right)\right)$ [a]	$C_j = 200 + 600 \bullet \left(1 - exp\left(-0.01612 \bullet \dot{Q}_{DHW}^{max}\right)\right)$ [a]	Application of Ecopassport UNIC−00022-V02.01-EN [b]	22
Absorption chiller	$C_0 = 6671 \bullet \dot{Q}_{sorp}^{ev\ 0.430} + 3669 \bullet \dot{Q}_{sorp}^{ev\ 0.730}$ (gear & installation) [c]	$C_j = 2.628 \times 10^{-2} \bullet \dot{Q}_{cooling}^{max\ 0.490} \bullet t_{eq}$ With $t_{eq} = \frac{Q_{cooling}}{\dot{Q}_{cooling}^{max}}$ duration of operation [h] [d]	$\Gamma = 217.3 \bullet \dot{Q}_{sorp}^{ev}$ [e]	20 [h]
Air-cooled chiller	$C_0 = 1167.9 \bullet \dot{Q}_{ASHP}^{cond\ 0.834}$ [63]	$C_j = 250$; $C_{11} = 704 + 105.73 \bullet \dot{Q}_{ASHP}^{cond}$ (replacement of compressor at year 11) [63]	Application of Ecopassport UNIC−00039-V01.01-FR [b]	22
Cooling Tower	$C_0 = 0.32 \bullet \dot{m}_{air,CT}^{max}$ [f]	$C_j = 0.03 \bullet C_0$	$\Gamma = 0.76 \bullet \dot{m}_{air,CT}^{max}$ [g]	20
Buried twin pipes	Cost of one pipe (SDR = 11) without insulation [€.m^{-1}]: $c_p = 8.104 \bullet e_p + 1.081 \bullet d_{int,p} + 12584 \bullet e_p \bullet d_{int,p} + 274.1 \bullet d_{int,p}^2$ Additional cost for insulation [€.m^{-1}]: $c_{insul} = 9848 \bullet \frac{\pi}{4} \bullet \left(d_{casing}^2 - 2d_{ext,p}^2\right)$ Network layout, including pipe handling, ground excavation and sand backfilling [€.m^{-1}] (assuming a trench section is 1 m^2): $c_{layout} = 55$ Cost [€] of a section of length L [m]: $C_0 = L \bullet \left(c_{layout} + c_{insul} + 2 \bullet c_{pipe}\right)$	$C_j = 0$	Only emissions related to the raw material and manufacturing and casing are considered. PE (one pipe) [kgCO2eq.m^{-1}]: $\gamma_{PE} = \gamma_{PE,M} \bullet \rho_{PE} \bullet \pi \bullet \left(d_{int,p} \bullet e_p + e_p^2\right)$ Insulation (one pipe) [kgCO2eq.m^{-1}] (regression on data from [64]): $\gamma_{insul} = 8330 \bullet \frac{\pi}{4} \bullet \left(d_{casing}^2 - 2d_{ext,p}^2\right)$ For a section of length L [m]: $\Gamma = L \bullet (2\gamma_{PE} + \gamma_{insul})$ $\rho_{PE} = 950$ kg.m^{-3}: PE density $\gamma_{PE,M} = 3.90$ kgCO2eq.kg^{-1} [h]	50
Geothermal wells	$I = 1.9 \bullet 10^6$ [i]	$C_j = 50 \bullet 10^3$	Not taken into account since the GWP is site-specific.	50

[a] Source: regressions established on the data provided by http://www.prix-construction.info
[b] Refers to *Profils Environnementaux de Produits* (PEP) Ecopassport, available at https://register.pep-ecopassport.org/pep/consult
[c] Regression on 45 machine costs. Personal communications from manufacturers.
[d] Source: Adapted from [65]
[e] Source: [66], for a LiBr-H_2O single-effect absorption chiller, similar to the chiller considered in this paper.
[f] Typical investment cost is often assumed to be 150 € per "cooling tower ton" (i.e. per 4.396 kW).
[g] Source: [67] studied a CT operating 8760 h/y in Germany for 20 years. The electricity in usage stage accounted for 90% of the total GWP. Based on the paper, the GWP of the Raw material and manufacturing per air flow rate is estimated to be 0.76 kgCO_2eq/(kg.h^{-1}). The energy for the wastewater treatment and the fresh water demand is not taken into account here, neither the demand for freshwater.
[h] Source: Base Carbone by French Energy Agency ADEME (https://base-impacts.ademe.fr)
[i] Source: [68] p 104. The investment estimated in 2011 has been increased by 19% to take into account inflation [69].

energy costs (see Fig. 16b). Note that the difference of cost between the geothermal system and the *status quo* could be cleared by a subsidy s defined by Eq. (39):

$$s = \frac{c - c_{statu\ quo}}{\gamma_{statu\ quo} - \gamma} \tag{39}$$

Here $s = \frac{37.5-33.2}{170.1-103.1} = 70$ € per avoided ton CO_2eq. This is a relatively low value since, for example, the advisory board of the French Prime Minister sets a reference value for the CO_2eq ton (in € of 2018) at 54€ in 2018, 250€ in 2030, then 500€ in 2050, and finally 775€ in 2050 [70]. For both the geothermal system and the *status quo*, the energy represents 90 to 95% of the GWP.

4.3. Influence of the scenario parameters upon the trade-off

Several alternative scenarios have been considered to investigate the influence of the input parameters upon the Pareto front (see Fig. 17a-e). For every scenario, the system undergoes multi-objective optimization. The normalized share of cooling from absorption chiller $Q_{sorp}^{ev\ \sim}$ and electricity consumption W_{el}^{*} at the trade-off (defined by Eq. (38)) are reported in Fig. 18. Note that both values originate from the TRNSYS model evaluated after the optimization. There are little discrepancies between the predictions and the "true" values of W_{el}^{*} as computed by TRNSYS, both values being in good agreement (see Fig. 13b). At the trade-off points, the following trends appear:

- *Thermal demand* (see Fig. 17a): Decreasing the cooling demand to 1.5 MW (and the DHW demand accordingly) results in an increase of the cost, as illustrated by the Pareto front moving to the right. A lower demand increases the capital-intensive equipment costs (mainly sorption machine and geothermal wells), maintenance, and equipment per amount of delivered energy.
- *Buried pipe length* (see Fig. 17b): The remoteness of the end consumer dramatically increases both the cost and GWP, even for relatively small distances, e.g., $L = 1650$ m ($q_\ell^{-1} = 0.15$ m.MWh^{-1}). The total cost c reaches 41.9 €.MWh^{-1}. The cost of the buried pipes including its installation reaches 1310 €.ml^{-1} and accounts for 16% of c. The remoteness drastically increases the electricity consumption, due to an increased consumption of the ACC rather than the circulation pumps P_1 and P_2. Meanwhile, $Q_{sorp}^{ev\ \sim}$ is almost halved compared to the reference scenario. Remoteness appears as a major obstacle to the system deployment. Only a subsidy as defined in eq. *(39)* reaching 220 € per avoided ton CO_2eq could make the system profitable compared to the *status quo*.
- *Geothermal temperature* (see Fig. 17c): Increasing T_{GTH} dramatically increases the amount of cooling (and the absorption chiller's COP) provided by the absorption chiller, decreasing both the cost and GWP at the trade-off. A similar behavior is observed for solar-driven

absorption chillers [71], for which it is more a problem to overcome since the solar irradiation drives the temperature level of the driving source temperature [72]. Indeed, for these systems, the low driving temperature available in the morning limits the cooling generation capacity, which might be a problem for some applications. In the case of the present work, the increased cooling capacity available at high driving temperatures decreases the need of the ACC, also decreasing the electricity consumption. To avoid LiBr crystallization, the generator inlet temperature is not allowed to exceed a critical value in the range 85–95 °C (see eq. (8)). Warmer fluid is recirculated. Consequently the marginal gain in $Q_{sorp}^{ev\ \sim}$ tends to decrease when the geothermal temperature increases (see Fig. 18). Note that a previous economical assessment of geothermal absorption chiller by Wang et al. did not investigate the effect of the temperature [8], though it appears to be a significant parameter.

- *Geothermal flow-rate* (see Fig. 17d): A similar trend than for the driving heat temperature is observed when $\dot{m}_{GTH}$ increases from 100 ton.h^{-1} to 200 ton.h^{-1}, though the effect on $Q_{sorp}^{ev\ \sim}$ and $W_{el}^{\ *}$ is much smaller. This is mainly due to the limited impact of the heat transfer fluid flow rate on the heat transfer coefficient of the generator, while the maximum heat transfer rate is limited by the temperature of the heat transfer fluid [73].
- *Ratio of DHW* (*see* Fig. 17e): The energy cost of the status quo decreases when the ratio of DHW r_{DHW} decreases since a smaller amount of rather expensive oil is used (for DHW preparation) in the final energy mix. By contrast, the cost of the geothermal sorption system increases with a decrease of DHW r_{DHW} since the equipment and maintenance costs are no more allocated to the DHW needs. Regarding the GWP, since less fuel per MWh is burned when r_{DHW} decreases, the relative advantage of cooling and DHW cogeneration from the geothermal absorption chiller decreases.
- Cooling set point temperature $T_{sp\ cooling}$ (see Fig. 17f): The GWP and cost of the system is highly sensitive to the setpoint cooling temperature. Indeed, even a small increase of $T_{sp\ cooling}$ (e.g., 2–3 °C) dramatically increases the absorption chiller production (and the sorption chiller's COP), decreasing both the electricity consumption and the energy cost.

Finally, from Fig. 17, one can clearly observe the trends highlighted through Fig. 16. Indeed, one can see that a higher driving temperature is ideal to increase the cooling capacity (and reduce the electricity consumption that a backup ACC would demand). On the other hand, increasing the geothermal heat transfer fluid flow rate and the setpoint cooling temperature also increases the cooling capacity while decreasing the electricity consumption. Furthermore, the most of the electricity consumed in the studied configurations comes from the backup ACC. Even though the variation of the different studied parameters impact the normalized electricity consumption, their impact remains small compared with the consumption of the ACC, which dominates the trend.

5. Conclusions

This paper has introduced a system combining a geothermal single-effect absorption chiller and a heat exchanger for cooling and Domestic Hot Water production in tropical climates. The dynamic simulation of the system shows that the cooling production of the absorption chiller depends upon the weather conditions. Furthermore, the temperature of the geothermal resource, its flow rate, and the nominal capacity of the absorption chiller are the most significant parameters impacting the electricity consumption of the system and the share of cooling delivered by the absorption chiller.

After a stage of surrogate modelling, the system undergoes a multi-objective optimization to minimize both the cost and the Global Warming Potential of the delivered thermal energy. Several scenarios are considered taking into account the energy mix and economic context of a French Caribbean Island where most electricity is generated from fossil fuels. The following trends are observed:

a) Without any subsidy, the system turns out to be systematically more expensive than a combination of a classical vapor compression chiller and a boiler for DHW preparation. However, the GWP of the provided energy can be significantly diminished.
b) The proximity of the geothermal well, large cooling powers (here 2 MWth), and the use of the warm water leaving the sorption generator (here for DHW production) appear to be key factors for the system relevance.
c) Even though a single-stage absorption chiller can operate with a geothermal fluid as low as 70 °C, hotter geothermal resources (e.g., 100–110 °C) dramatically increase the economic viability and should be therefore looked for. The cost and GWP, however, are less sensitive to the geothermal flow rate.
d) The equipment of buildings with cooling emitters operating at 10 °C instead of 7 °C can increase the system profitability as well.

It should be emphasized that a hotel has been considered for this study. This building exhibits a high cooling requirement throughout the year since cooling is required day and night; the equivalent duration of cooling is as high as $t_{eq\ cooling} = Q_{cooling}/\dot{Q}_{cooling}^{max} = 570{,}500/104.3 = 5470$ h.y^{-1}. In-situ monitoring of office buildings shows they tend to exhibit much lower, or even zero, cooling needs at night and large cooling peaks, which decreases $t_{eq\ cooling}$ [2]. The supply of those buildings, though not investigated in this paper, may lead to a high initial investment per amount of delivered thermal energy and subsequent high energy costs.

Further research may focus on integrating solar thermal collectors to warm the geothermal fluid before feeding the absorption chiller. Besides, it would be relevant to compare the system with an Organic Ranking Cycle generating electricity directly from the geothermal resource.

CRediT authorship contribution statement

Charles Maragna: Writing – review & editing, Writing – original draft, Validation, Supervision, Methodology, Investigation, Formal analysis, Conceptualization. **Amín Altamirano:** Writing – review & editing, Writing – original draft, Validation, Investigation, Formal analysis. **Brice Tréméac:** Writing – review & editing. **Florent Fabre:** Investigation. **Laurène Rouzic:** Investigation. **Pierre Barcellini:** Investigation.

Declaration of competing interest

The authors declare that they have no known competing financial interests or personal relationships that could have appeared to influence the work reported in this paper.

Data availability

Data will be made available on request.

Acknowledgements

The authors would like to thank INTERREG Caraïbes program for its financial support. The ETC ("Energy Transition in the Caribbean") project is cofounded by the INTERREG Caraïbes program under the umbrella of the European Regional Development Fund (ERDF). This paper would not have been possible without their support.

The main author thanks Sergei Manzhos from Tokyo Tech for providing the Matlab code for High Dimensional Gaussian Processes (though not reported in this paper) and discussions, and Jérémy Rohmer from BRGM for in-depth explanations and discussions about Gaussian Processes.

The authors would like to thank the three anonymous reviewers.

Appendix A. Gaussian processes: Theoretical background

To build the surrogates, we adopt the framework of "Gaussian Processes" (GP). We wrote this section using the reference textbook from Rasmussen and Williams [74]. The function $y(\chi)$ is assumed to be a realization of a GP Y. Y is the sum of a deterministic, parametrized trend function $\mu(\chi)$, a centered square-integrable stochastic process Z and some noise ε:

$$Y(\chi) = \underbrace{\sum_{k=1}^{p} \beta_k f_k(\chi)}_{=\mu(\chi)} + Z(\chi) + \varepsilon \tag{40}$$

The f_k's appearing in $\mu(\chi)$ are some fixed basis functions and the β_k's are unknown real coefficients to be estimated. The noise is assumed to follow a normal distribution $\varepsilon \sim \mathcal{N}(0, \sigma_n)$, where σ_n is the noise standard deviation. Let us focus to the case where $\boldsymbol{\beta}$ is set to a constant ("*simple kriging*"), so that the GP captures the whole variation of the output $y(\chi)$. We set the noise to a negligible value ($\sigma_n \ll 1$) since we assume the model is purely deterministic: there is no "*nugget effect*". The GP construction is about deriving best linear predictions of Y. Z's covariance function, named "kernel" and denoted $k(.,.)$, can be written as:

$$\forall \chi_1, \chi_2, k(\chi_1, \chi_2) = {\sigma_f}^2 R(\chi_1, \chi_2) = cov(y_1, y_2) \tag{41}$$

Where *1* and *2* refer to two points of the training dataset, σ_f is a scale parameter known as the noise-free signal standard deviation and $R(.,.)$ the correlation function related to $k(.,.)$. A prediction $\widehat{Y}(\chi_{new})$ at a new observation point χ_{new} is:

$$\widehat{Y}(\chi_{new}) = \boldsymbol{k}_{new}{}^{\intercal} \boldsymbol{K}^{-1} \boldsymbol{y} \tag{42}$$

Where $\boldsymbol{k}_{new} = \boldsymbol{k}(\chi_{new})$ denotes the vector of covariances between the new point χ_{new} and the N training points and $\boldsymbol{K} = {\sigma_f}^2 \boldsymbol{R}$ is the covariance matrix for the training points, and $\boldsymbol{y}$ the output at the training points.

Kernels are functions parametrized by some "hyperparamaters". A Matérn3/2 kernel function was used since it is once differentiable, making it good at capturing physical processes. It reads:

$$k(\chi_1, \chi_2) = {\sigma_f}^2 \left(1 + \sqrt{3}\, r\right) exp\left(-\sqrt{3}\, r\right) \tag{43}$$

with:

$$r = r(\chi_1, \chi_2) = \sqrt{\sum_{i=1}^{D} \left(\frac{{\chi_i}^{(1)} - {\chi_i}^{(2)}}{\ell_i}\right)^2} \tag{44}$$

Where ℓ_i ($i = 1, \ldots, D$) is the correlation length for the predictor (variable) i. Such anisotropic kernels, i.e. kernels with independent correlation lengths per predictor, are sometimes referred to as "Automatic Relevance Determination" (ARD) kernels. The correlation lengths briefly define how far apart the input values χ_i can be for the response values to become uncorrelated. The GP is fitted with the built-in MATLAB *fitrgp* function. This function determines the most relevant set of hyperparameter (here the standard deviation σ_f and correlations lengths ℓ_i) by maximizing the Log Marginal Likelihood (LML) function [51] which reads as follows under simple kriging and no-nugget-effect assumptions:

$$\mathrm{LML}\left(\sigma_f, \ell_1, \ldots, \ell_D\right) = -\frac{1}{2} log(\mathrm{Tr}(\boldsymbol{K})) - \frac{1}{2} \boldsymbol{y}^{\intercal} \boldsymbol{K}^{-1} \boldsymbol{y} - \frac{N}{2} log(2\pi) \tag{45}$$

In Eqn 45, $\mathrm{Tr}(\boldsymbol{K})$ accounts for the trace (i.e. the sum of elements on the main diagonal) of matrix $\boldsymbol{K}$. Classical properties of Gaussian Processes include the fact that the estimation of the output at a new point $\widehat{Y}(\chi)$ interpolates the data, provided that no nugget effect is included. Cross-validation is necessary to estimate the quality of the surrogate. Cross-validation is a procedure where a part $1/n$ of the data is randomly selected and left apart (here $n = 5$), acting as a test sample [55]. A surrogate is fitted on a fraction $(1–1/n)$ of the sample and the procedure is repeated n times by permuting the samples. The metric for the estimation of the quality of the surrogate of a function f is often chosen to be the Root Mean Square Error (RMSE):

$$RMSE(f) = \left(\sum_{i=1}^{N} \frac{\left[(f)_{data} - (f)_{surrogate} \right]^2}{N} \right)^{1/2} \tag{46}$$

The construction of GP with high dimensional data sets, which is the case here ($D = 17$), can be challenging [53,54]. The reader is referred to [52]

for an overview of approaches to build high-dimensional GP and e.g. to [75] for methods to iteratively sample the function of interest.

Appendix B. Interpretation of Gaussian Processes for W_{el}^{*} and $Q_{sorp}^{ev\ \sim}$

One advantage of GPs is their interpretability. Each variable i is associated with a correlation length ℓ_i determined during the GP fitting (i.e. optimization of Eqn 45), which briefly defines how far apart the input values χ_i can be for the response values to become uncorrelated (see Appendix A). In the case of simple kriging, smaller ℓ_i are associated with a variable i having a larger influence. As ℓi can change by several orders of magnitude, it is better to plot $\frac{1/\ell i}{\sum_{i=1}^{D} 1/\ell i}$ to qualitatively compare the weights of each variable (see Fig. 19). For both W_{el}^{*} and $Q_{sorp}^{ev\ \sim}$, the specific geothermal flow rate $\dot{m}_{GTH}/\dot{Q}_{cooling}^{max}$, the geothermal temperature T_{GTH} and the normalized nominal power of the absorption chiller $\dot{Q}_{sorp}^{ev\ *}$ are the most significant input parameters. This is qualitatively in line with the sensitivity analysis reported in §3.3.

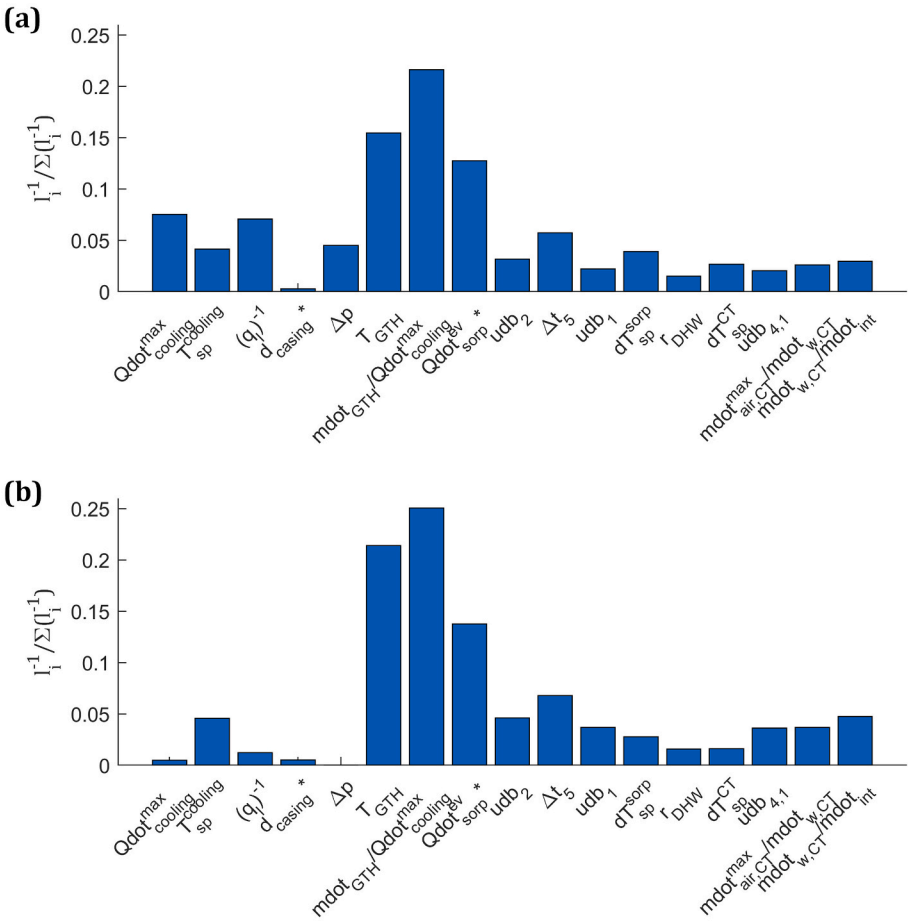

Fig. 19. Weight of each variable i upon (a) normalized electric consumption of the system W_{el}^{*}, (b) normalized amount of cooling produced by the absorption chiller $Q_{sorp}^{ev\ \sim}$.

Appendix C. System characteristics on the trade-offs

	Scenario parameters						Design variables (i.e. results of optimization at the trade-off)											Objectives	
Parameter	$\dot{Q}_{cooling}^{max}$	$T_{sp\ cooling}$	r_{DHW}	L	T_{GTH}	$\dot{m}_{GTH}$	Δt_5	$\dot{Q}_{sorp}^{ev\ *}$	$\dot{m}_{air,CT}^{max}/\dot{m}_{w,CT}$	$\dot{m}_{w,CT}/\dot{m}_{int}$	udb_2	udb_1	dT_{sp}^{sorp}	dT_{sp}^{CT}	$udb_{4,1}$	d_{casing}*	Δp	c	γ
Unit	MW	°C	–	m	°C	ton.h^{-1}	h	–	–	–	°C	°C	°C	°C	°C	–	Pa.m^{-1}	€.MWh^{-1}	kgCO$_2$eq.MWh^{-1}
Base.	2.0	7	1.0	0	80	100	1.41	0.77	3.00	0.54	−0.50	3.00	0.00	2.00	3.00			37.5	103.1
A1	1.5	7	1.0	0	80	100	1.50	0.91	3.00	0.50	−0.50	3.00	0.00	2.10	3.10			43.2	89.1
B1	2.0	7	1.0	1650	80	100	0.25	0.32	2.35	1.30	−0.50	6.57	0.00	2.00	3.00	2.50	51.80	41.9	130.6
B2	2.0	7	1.0	3300	80	100	0.25	0.25	2.44	1.27	−0.50	7.00	0.00	2.00	3.00	2.50	62.24	45.7	143.4
C3	2.0	7	1.0	0	85	100	1.57	0.81	3.00	0.55	−0.50	3.92	0.00	2.44	3.44			37.0	87.8
C4	2.0	7	1.0	0	90	100	1.68	0.81	3.00	0.59	−0.50	4.94	0.00	2.81	3.81			36.4	75.3
C5	2.0	7	1.0	0	95	100	1.77	0.80	3.00	0.62	−0.50	5.55	0.00	3.06	4.06			36.0	65.5
C6	2.0	7	1.0	0	100	100	1.89	0.80	3.00	0.61	−0.54	5.72	0.00	3.19	4.19			35.7	58.8
C7	2.0	7	1.0	0	105	100	2.08	0.83	3.00	0.53	−0.65	5.48	0.00	3.26	4.26			35.6	54.4
D1	2.0	7	1.0	0	80	125	1.57	0.85	3.00	0.50	−0.50	3.00	0.00	2.01	3.01			37.8	95.0
D2	2.0	7	1.0	0	80	150	1.63	0.90	3.00	0.50	−0.50	3.07	0.00	2.06	3.06			38.1	89.4
D3	2.0	7	1.0	0	80	175	1.66	0.89	3.00	0.50	−0.50	3.23	0.00	2.09	3.09			38.0	85.9
D4	2.0	7	1.0	0	80	200	1.67	0.92	3.00	0.50	−0.50	3.38	0.00	2.10	3.10			38.3	83.2
E1	2.0	7	0.0	0	80	100	1.41	0.74	3.00	0.54	−0.50	3.49	0.00	2.00	3.00			43.3	118.9
E2	2.0	7	0.2	0	80	100	1.41	0.74	3.00	0.54	−0.50	3.36	0.00	2.00	3.00			42.0	115.5
E3	2.0	7	0.4	0	80	100	1.41	0.75	3.00	0.54	−0.50	3.24	0.00	2.00	3.00			40.8	112.3
E4	2.0	7	0.6	0	80	100	1.41	0.76	3.00	0.54	−0.50	3.13	0.00	2.00	3.00			39.6	109.2
E5	2.0	7	0.8	0	80	100	1.41	0.77	3.00	0.54	−0.50	3.02	0.00	2.00	3.00			38.6	105.8
F1	2.0	8	1.0	0	80	100	1.55	0.78	3.00	0.53	−0.50	3.00	0.00	2.00	3.00			36.8	93.0
F2	2.0	9	1.0	0	80	100	1.74	0.80	3.00	0.51	−0.50	3.00	0.21	2.00	3.00			36.3	85.1
F3	2.0	10	1.0	0	80	100	1.93	0.81	3.00	0.50	−0.52	3.00	0.50	2.00	3.00			35.8	78.8
F4	2.0	11	1.0	0	80	100	2.17	0.80	3.00	0.50	-0.63	3.00	0.78	2.00	3.00			35.3	74.2
F5	2.0	12	1.0	0	80	100	2.33	0.79	3.00	0.50	-0.68	3.00	0.98	2.00	3.00			34.9	71.2

Appendix D. Supplementary data

Supplementary data to this article can be found online at https://doi.org/10.1016/j.apenergy.2024.123102.

References

[1] International Energy Agency. The future of cooling. 2018.
[2] Artelya. REX des consommations d'électricité des bâtiments tertiaires à La Réunion et en Guadeloupe. Rapport Phase 3 : Synthèse des audits Guadeloupe. PACTE / ADEME Direction Régionale Guadeloupe; 2020.
[3] B. Sanjuan, C. Dezayes, C. Maragna, Potentialités géothermiques des Zones Non Interconnectées (ZNI) de l'Outre-mer français, BRGM, n.d. http://ficheinfoterre.brgm.fr/document/RP-72887-FR.
[4] Almasri RA, Abu-Hamdeh NH, Esmaeil KK, Suyambazhahan S. Thermal solar sorption cooling systems, a review of principle, technology, and applications. Alex Eng J 2022;61:367–402. https://doi.org/10.1016/j.aej.2021.06.005.
[5] Altamirano A, Maragna C, Tremeac B. Commercial Sorption Chillers for the Valorization of Low-Temperature Renewable heat Sources: Technical Review, in: Paris. 2023. https://doi.org/10.18462/iir.icr.2023.0215.
[6] Hugo V, Flores F, Román JC, Alpírez GM. Performance analysis of different working fluids for an absorption refrigeration cycle. Am J Environ Eng 2014;4:1–10. https://doi.org/10.5923/s.ajee.201401.01.
[7] Altamirano A, Pierrès NL, Stutz B. Review of small-capacity single-stage continuous absorption systems operating on binary working fluids for cooling : Theoretical, experimental and commercial cycles Synthèse des systèmes mono-étagés d ' absorption continue de faible puissance fonctionnan. Int J Refrigerat 2019;106:350–73. https://doi.org/10.1016/j.ijrefrig.2019.06.033.
[8] Wang X, Bierwirth A, Christ A, Whittaker P, Regenauer-Lieb K, Chua HT. Application of geothermal absorption air-conditioning system: A case study. Appl Therm Eng 2013;50:71–80. https://doi.org/10.1016/j.applthermaleng.2012.05.011.
[9] Han B, Li WJ, Li M, Liu L, Song J. Study on Libr/H2O absorption cooling system based on enhanced geothermal system for data center. Energy Rep 2020;6:1090–8. https://doi.org/10.1016/j.egyr.2020.11.072.
[10] Tetemke Y, Paramasivam V, Tadele F, Selvaraj SK. Analyzed of vapor absorption refrigeration systems powered by geothermal energy: site in Ethiopia. Mater Today: Proc 2021;46:7570–80. https://doi.org/10.1016/j.matpr.2021.01.642.
[11] Saucedo-Velázquez J, Gutiérrez-Urueta G, Wong-Loya JA, Molina-Rodea R, Franco WRG. Cooling potential for single and advanced absorption cooling systems in a geothermal field in Mexico. Processes 2022;10. https://doi.org/10.3390/pr10030583.
[12] Holdmann G, Springs CH. Absorption chiller for the chena hot springs aurora ice museum. https://www.google.com/url?sa=t&rct=j&q=&esrc=s&source=web&cd=&ved=2ahUKEwiTncH6ruf6AhUCx4UKHRDVA18QFnoECAkQAQ&url=https%3A%2F%2Fwww.osti.gov%2Fservlets%2Fpurl%2F1209255&usg=AOvVaw2UY4OLQaxmyp7IZFRW9oud; 2006.
[13] Gado MG, Ookawara S, Nada S, El-Sharkawy II. Hybrid sorption-vapor compression cooling systems: A comprehensive overview. Renew Sustain Energy Rev 2021;143:110912. https://doi.org/10.1016/j.rser.2021.110912.
[14] Khosravi A, Syri S. Modeling of geothermal power system equipped with absorption refrigeration and solar energy using multilayer perceptron neural network optimized with imperialist competitive algorithm. J Clean Prod 2020;276:124216. https://doi.org/10.1016/j.jclepro.2020.124216.
[15] Ghiasirad H, Asgari N, Khoshbakhti Saray R, Mirmasoumi S. Thermoeconomic assessment of a geothermal based combined cooling, heating, and power system, integrated with a humidification-dehumidification desalination unit and an absorption heat transformer. Energ Conver Manage 2021;235:113969. https://doi.org/10.1016/j.enconman.2021.113969.
[16] Al-Hamed KHM, Dincer I. Investigation of a concentrated solar-geothermal integrated system with a combined ejector-absorption refrigeration cycle for a small community. Int J Refrigerat 2019;106:407–26. https://doi.org/10.1016/j.ijrefrig.2019.06.026.
[17] Yilmaz C. Thermodynamic and economic investigation of geothermal powered absorption cooling system for buildings. Geothermics 2017;70:239–48. https://doi.org/10.1016/j.geothermics.2017.06.009.
[18] Xu A, Xu M, Xie N, Xiong Y, Huang J, Cai Y, et al. Thermodynamic analysis of a hybrid system coupled cooling, heating and liquid dehumidification powered by geothermal energy. Energies 2021;14. https://doi.org/10.3390/en14196084.
[19] Kordlar MA, Heberle F, Brüggemann D. Evaluation and optimization of the annual performance of a novel tri-generation system driven by geothermal brine in off-design conditions. Appl Sci (Switzerland) 2020;10. https://doi.org/10.3390/APP10186532.
[20] Calise F, Cappiello FL, d'Accadia MD, Vicidomini M. Thermo-economic analysis of hybrid solar-geothermal polygeneration plants in different configurations. Energies 2020;13. https://doi.org/10.3390/en13092391.
[21] Zhang F, Yan Y, Liao G, J. E. Energy, exergy, exergoeconomic and exergoenvironmental analysis on a novel parallel double-effect absorption power cycle driven by the geothermal resource. Energ Conver Manage 2022;258:115473. https://doi.org/10.1016/j.enconman.2022.115473.
[22] Javanshir N, Seyed Mahmoudi SM, Kordlar MA, Rosen MA. Energy and cost analysis and optimization of a geothermal-based cogeneration cycle using an ammonia-water solution: thermodynamic and thermoeconomic viewpoints. Sustainability (Switzerland) 2020;12. https://doi.org/10.3390/su12020484.
[23] TRNSYS: A TRaNsient SYstems simulation program, (n.d.). https://sel.me.wisc.edu/trnsys/index.html.
[24] University of Wisconsin–Madison. Solar energy laboratory, TRNSYS, a transient simulation program. Madison, Wis: The Laboratory; 1975. 1975. https://search.library.wisc.edu/catalog/999800551102121.
[25] TESS Component library package, (n.d.). https://www.trnsys.com/tess-libraries/.
[26] Giraud L, Paulus C, Baviere R. Modeling of solar district heating: A comparison between TRNSYS and MODELICA. In: Proceedings of the EuroSun 2014 Conference, International Solar Energy Society, Aix-les-Bains, France; 2015. p. 1–11. https://doi.org/10.18086/eurosun.2014.19.06.
[27] Dempsey M. Dymola for multi-engineering modelling and simulation. In: 2006 IEEE Vehicle Power and Propulsion Conference; 2006. p. 1–6. https://doi.org/10.1109/VPPC.2006.364294.
[28] Sanjuan B, Genter A, Correira H, Girard J-P, Roig J-Y, Brach M. Travaux scientifiques associés à la réalisation des trois puits d'exploration géothermique dans la plaine du Lamentin (Martinique). http://infoterre.brgm.fr/rapports/RP-51671-FR.pdf; 2002.
[29] Marchio D, Reboux P. Introduction aux Transferts Thermiques, Paris. 2003.
[30] SIA. Norme Suisse. Sondes géothermiques. SIA 384/6, Société suisse des ingénieurs et des architectes, Zurich. 2010.
[31] Yazaki, Water-Fired Chiller/Chiller-Heater, (n.d.). http://www.yazakienergy.com/docs/WFCSUL-SBDG1-2C1-0115.pdf (accessed February 28, 2023).
[32] Altamirano A, Le Pierrès N, Stutz B, Coronas A. Performance characterization methods for absorption chillers applied to an NH3-LiNO3 single-stage prototype. Appl Therm Eng 2021;185:116435. https://doi.org/10.1016/j.applthermaleng.2020.116435.
[33] Altamirano A, Maragna C, Tremeac B. Implementation of adapted black box models for the performance characterization of commercial sorption chillers. In: Kassel, Germany; 2022. https://proceedings.ises.org/paper/eurosun2022/eurosun2022-0168-Altamirano.pdf.
[34] Altamirano Cundapí A, Stutz B, Le Pierrès N. Selection of high-performance working fluid for a solar-geothermal absorption cooling system and techno-economic study in the northern mexican conditions. In: Proceedings of EuroSun 2018, International Solar Energy Society, Rapperswil, CH; 2018. p. 1–12. https://doi.org/10.18086/eurosun2018.04.15.
[35] Yuan Z, Herold KE. Thermodynamic properties of aqueous lithium bromide using a multiproperty free energy correlation. HVAC&R Res 2005;11:377–93. https://doi.org/10.1080/10789669.2005.10391144.
[36] Boryta DA. Solubility of lithium bromide in water between −50.deg. and +100. deg. (45 to 70% lithium bromide). J Chem Eng Data 1970;15:142–4. https://doi.org/10.1021/je60044a030.
[37] ASHRAE. 2020 ASHRAE Handbook - HVAC systems and equipment, in. 2021.
[38] Baker Donald R, Shryock HA. A comprehensive approach to the analysis of cooling tower performance. J Heat Transfer 1961;88:339–49. https://doi.org/10.1115/1.3682276.
[39] Kloppers JC, Kröger DG. A critical investigation into the heat and mass transfer analysis of counterflow wet-cooling towers. Int J Heat Mass Transf 2005;48:765–77. https://doi.org/10.1016/j.ijheatmasstransfer.2004.09.004.
[40] Variable flow over cooling towers for energy savings. SPX COOLING TECHNOLOGIES, INC; 2017. https://spxcooling.com/wp-content/uploads/TR-014.pdf.
[41] Kuehn TH. J.W. (viaf)3764742 Ramsey, J.L.T. Environmental engineering. Threlkeld. 3rd ed. Upper Saddle River: Thermal environmental engineering; 1998. http://lib.ugent.be/catalog/rug01:000801719.
[42] Costelloe B, Finn DP. Heat transfer correlations for low approach evaporative cooling systems in buildings. Appl Therm Eng 2009;29:105–15. https://doi.org/10.1016/j.applthermaleng.2008.02.005.
[43] Bernier MA. Cooling tower performance: Theory and experiments. https://www.osti.gov/biblio/33238; 1994.
[44] Gharagheizi F, Hayati R, Fatemi S. Experimental study on the performance of mechanical cooling tower with two types of film packing. Energ Conver Manage 2007;48:277–80. https://doi.org/10.1016/j.enconman.2006.04.002.
[45] Navarro P, Ruiz J, Hernández M, Kaiser AS, Lucas M. Critical evaluation of the thermal performance analysis of a new cooling tower prototype. Appl Therm Eng 2022;213:118719. https://doi.org/10.1016/j.applthermaleng.2022.118719.
[46] Ruiz J, Navarro P, Hernández M, Lucas M, Kaiser AS. Thermal performance and emissions analysis of a new cooling tower prototype. Appl Therm Eng 2022;206:118065. https://doi.org/10.1016/j.applthermaleng.2022.118065.
[47] Lucas M, Ruiz J, Martínez PJ, Kaiser AS, Viedma A, Zamora B. Experimental study on the performance of a mechanical cooling tower fitted with different types of water distribution systems and drift eliminators. Appl Therm Eng 2013;50:282–92. https://doi.org/10.1016/j.applthermaleng.2012.06.030.
[48] Air cooled screw chillers, LG HVAC SOLUTION, n.d. https://www.lg.com/global/business/download/resources/sac/Catalogue_Air_Cooled_Screw_ENG_F.pdf (accessed January 10, 2023).
[49] Maragna C, Rey C, Perreaux M. A novel and versatile solar borehole thermal energy storage assisted by a heat pump. Part 1: system description. Renew Energy 2023;208:709–25. https://doi.org/10.1016/j.renene.2023.03.105.

[50] Westermann P, Evins R. Surrogate modelling for sustainable building design – A review. Energ Buildings 2019;198:170–86. https://doi.org/10.1016/j.enbuild.2019.05.057.
[51] Roustant O, Ginsbourger D, Deville Y. DiceKriging, DiceOptim: two R packages for the analysis of computer experiments by kriging-based metamodeling and optimization. J Stat Softw 2012;51:1–55. https://doi.org/10.18637/jss.v051.i01.
[52] Binois M, Wycoff N. A survey on high-dimensional Gaussian process modeling with application to Bayesian optimization. ACM Trans Evol Learn Optim 2022;2:1–26. https://doi.org/10.1145/3545611.
[53] Manzhos S, Ihara M. Optimization of hyperparameters of Gaussian process regression with the help of a low-order high-dimensional model representation: application to a potential energy surface. J Math Chem 2023;61:7–20. https://doi.org/10.1007/s10910-022-01407-x.
[54] Karvonen T, Oates CJ. Maximum likelihood estimation in Gaussian process regression is Ill-Posed. 2023. http://arxiv.org/abs/2203.09179 (accessed June 7, 2023).
[55] Hastie T, Tibshirani R, Friedman J. The elements of statistical learning. New York, NY: Springer New York; 2009. https://doi.org/10.1007/978-0-387-84858-7.
[56] McKay MD, Beckman RJ, Conover WJ. A comparison of three methods for selecting values of input variables in the analysis of output from a computer code. Technometrics 1979;21:239–45. https://doi.org/10.2307/1268522.
[57] Don Mahawattege A. Prix de l' électricité en France et dans l' Union européenne en 2020. In: French Ministry of Ecology and Sustainable Development; 2021.
[58] Don Mahawattege A. Prix du gaz naturel en France et dans l'Union européenne en 2020. French Ministry of Ecology and Sustainable Development; 2021.
[59] French Ministry of Ecological Transition. Arrêté du 4 août 2021 relatif aux exigences de performance énergétique et environnementale des constructions de bâtiments en France métropolitaine et portant approbation de la méthode de calcul prévue à l'article R. 172–6 du code de la construction et de l'habitation. https://www.legifrance.gouv.fr/download/pdf?id=LBxKOX3Duk3h0j_ck_WBwvf9HBYDu3aSYhPKEIm97w4=; 2021.
[60] Mathworks, Design Optimization of a Welded Beam, (n.d.). https://fr.mathworks.com/help/gads/multiobjective-optimization-welded-beam.html (accessed December 8, 2022).
[61] Custódio AL, Madeira JFA, Vaz AIF, Vicente LN. Direct multisearch for multiobjective optimization. SIAM J Optimiz 2011;21:1109–40. https://doi.org/10.1137/10079731X.
[62] ADEME, Centre de ressources sur les bilans de gaz à effet de serre, (n.d.). https://bilans-ges.ademe.fr (accessed July 1, 2022).
[63] Ruffino E, Piga B, Casasso A, Sethi R. Heat pumps, wood biomass and fossil fuel solutions in the renovation of buildings: A techno-economic analysis applied to piedmont region (NW Italy). Energies 2022;15:2375. https://doi.org/10.3390/en15072375.
[64] Fröling M, Holmgren C, Svanström M. Life cycle assessment of the district heat distribution system part 1: pipe production. Int J Life Cycle Assess 2004;9:130–6. https://doi.org/10.1007/BF02978572.
[65] Absorption Chillers for CHP Systems. U.S. Department of Energy. https://www.energy.gov/sites/prod/files/2017/06/f35/CHP-Absorption%20Chiller-compliant.pdf; 2017.
[66] Hang Y, Qu M, Zhao F. Economical and environmental assessment of an optimized solar cooling system for a medium-sized benchmark office building in Los Angeles, California. Renew Energy 2011;36:648–58. https://doi.org/10.1016/j.renene.2010.08.005.
[67] Schulze C, Thiede S, Herrmann C. Life cycle assessment of industrial cooling towers. In: Schebek L, Herrmann C, Cerdas F, editors. Progress in life cycle assessment. Cham: Springer International Publishing; 2019. p. 135–46. https://doi.org/10.1007/978-3-319-92237-9_15.
[68] Gadalia A, Charni M, Fréchin N, Goyeneche O. Faisabilité et évaluation d'un programme de prospection et de valorisation géothermique en Martinique. Rapport Final 2011. http://ficheinfoterre.brgm.fr/document/RP-59690-FR.
[69] Taux d'inflation - Données annuelles de 1991 à 2022. INSEE; 2023. https://www.insee.fr/fr/statistiques/2122401#tableau-figure1.
[70] Quinet A. La valeur de l'action pour le climat. France Stratégie; 2019.
[71] Kerme ED, Chafidz A, Agboola OP, Orfi J, Fakeeha AH, Al-Fatesh AS. Energetic and exergetic analysis of solar-powered lithium bromide-water absorption cooling system. J Clean Prod 2017;151:60–73. https://doi.org/10.1016/j.jclepro.2017.03.060.
[72] Aliane A, Abboudi S, Seladji C, Guendouz B. An illustrated review on solar absorption cooling experimental studies. Renew Sustain Energy Rev 2016;65:443–58. https://doi.org/10.1016/j.rser.2016.07.012.
[73] Altamirano A, Stutz B, Le Pierrès N, Coronas A. Experimental characterization by thermal and mass effectivenesses of plate heat exchangers in NH3-LiNO3 absorption chillers. 2020. https://doi.org/10.14279/depositonce-10430.2.
[74] Rasmussen CE, Williams CKI. Gaussian processes for machine learning. Cambridge, Mass: MIT Press; 2006.
[75] Wang H, Li J. Adaptive Gaussian process approximation for Bayesian inference with expensive likelihood functions. 2018. http://arxiv.org/abs/1703.09930 (accessed March 23, 2023).